Deformation Mechanics of Quartz at a Single Asperity under Hydrothermal Conditions

by

Sudhish Kumar Bakku

B.Tech., Civil Engineering (2007)
Indian Institute of Technology Roorkee

Submitted to the Department of Earth Atmospheric and Planetary Sciences
in partial fulfillment of the requirements for the degree of

Master of Science in Geophysics

at the

MASSACHUSETTS INSTITUTE OF TECHNOLOGY

June 2010

Author .....
Department of Earth Atmospheric and Planetary Sciences
February 16, 2010

Certified by .....
Brian J. Evans
Professor
Thesis Supervisor

Accepted by .....
Maria Zuber
E. A. Griswold Professor of Geophysics,Department of Earth Atmospheric and Planetary Sciences

Deformation Mechanics of Quartz at a Single Asperity under Hydrothermal Conditions

by

Sudhish Kumar Bakku

Submitted to the Department of Earth Atmospheric and Planetary Sciences
on February 16, 2010, in partial fulfillment of the requirements for the degree of
Master of Science in Geophysics

Abstract

Pressure solution is a naturally occurring deformation process in fluid-bearing rocks, with implications for sediment consolidation rates and deformation in the mid to upper crust. The process involves dissolution at asperities under load; diffusion along grain-to-grain contacts; and precipitation in the pore space. The kinetics of the process and the identity of the rate-limiting step in quartzose rocks are still a subject of debate and depend critically upon the structure of the inter-granular boundary during deformation. To investigate the mechanisms and kinetics of pressure solution and the effects of changes in boundary morphology, we continuously monitored deformation and the evolution of boundary morphology at a Y-cut convex quartz lens that was pressed against a flat surface of Y-cut quartz under hydrothermal conditions (425^0C, 150 MPa fluid pressure, 80-435 MPa effective normal stress) in a see-through optical pressure vessel. The pore fluid was de-ionized water, which became saturated with quartz during the initial heat-up period. Several different boundary morphologies were used, including polished flats, etched and roughened flats, and an island-channel structure fabricated by plasma etching. The island-channel structure had square pillars of quartz, either 4μm or 8μm on a side, surrounded by an inter-connected grid of open channels of comparable width. Deformation at the interface between the quartz flat and lens (i.e., inter-granular convergence) was observed in only one case: the 4μm island-channel structure. In that instance, pillars within the contact region were eroded at a rate that decreased with time, and SEM photomicrographs after the experiment showed significant cataclasis within and adjacent to the pillars. The total transient convergence ($0.15\pm0.02\mu$m) observed during the 472 hour period was less than the original pillar height ($0.55\pm0.005\mu$m). For all surface morphologies, the shapes of the surface structures in both the loaded and unloaded regions evolved, perhaps owing to capillarity forces. Although an inter-connected island-channel structure was initially imposed upon some of the experiments, this open, fluid-filled boundary structure was seen to be a transient phenomenon that was largely destroyed during convergence. Thus, there was no evidence for a dynamically stable interface, as previously suggested.

Thesis Supervisor: Brian J. Evans
Title: Professor

Acknowledgments

I take this opportunity to express my gratitude to everyone who supported me, one way or the other, since I began my graduate studies at MIT. Your love, support and encouragement has made my experience here much more enjoyable and rewarding.

First and foremost, my sincere thanks to my advisor, Prof. Brian Evans, for showing faith in me and giving me this opportunity. His affable nature, constant encouragement at my success and an equal understanding at my failures has made my experience in lab much more rewarding.

I am very thankful to our collaborators, Dr. Stephan Hickman (USGS, Menlo Park), Prof. Yves Bernabé (MIT) and Dr. Nick Beeler (USGS, Vancouver). They have been a constant source of motivation and encouragement, especially, in those moments of despair. I appreciate their time and patience, in guiding me. In particular, the discussions with Prof. Yves Bernabé and Dr. Stephan Hickman were insightful and thought provoking. I am also thankful for their invaluable suggestions to the thesis. I thank Prof. Alison Malcolm for accepting to be on the defense committee.

I especially thank Dr. Ulrich Molk (MIT) and Brian Kilgore (USGS, Menlo Park) for helping me with issues in the lab and Dr. Usha Raghuram (SNF, Stanford) for helping me with the fabrication process at SNF; I thank my lab-mate, Alejandra Q Terminel, for helping me with the photo-lithography process.

I thank my labmates Nathaniel, Mirna, Alejandra and Hendrick for their company, support and invaluable friendship. I cherish the friendship of Vivek Raghunathan, Sumeet Kumar, Abishek Kashinath, Sami Alsaadan, Abdulaziz, Diego, Gabriela Melo, Nasruddin Nazerali, Bongani, Hussam, Yulia and many others at MIT. Special thanks to Carol A. Sprague, Kerin J. Willis and others at education office for making sure that I have a comfortable stay at MIT and taking care of me. I thank everyone for making me feel home at MIT and helping me remain sane at all times.

Most of all, I am greatly indebted to my parents, brother and family for their care and love. Thank you for believing in me and encouraging me at every step of my life.

Contents

List of Figures

List of Tables

Chapter 1

Introduction

1.1 Motivation

Rock deformation in the mid to upper crust is controlled by a variety of mechanisms including cataclastic processes such as fracturing or frictional grain sliding and rotation, and, relatively slow plastic processes like dislocation creep and pressure solution creep (Groshong, 1988). Pressure solution creep is a stress-enhanced, solution-transfer mechanism, that slowly dissipates the strain energy accumulated during sedimentation/burial/tectonic events. It involves dissolution at stressed, fluid-saturated, inter-granular contacts, diffusion along the contact and precipitation at relatively low stressed points in the pore space (see Figure 1-1). Pressure solution occurs at two different scales in nature: at the micro-scale, between grain-grain contacts (inter-granular pressure solution or IPS) and at the macro-scale, in the form of stylolites. Stylolites are insoluble seams of pyllosilicates that are thought to originate exclusively under non-hydrostatic conditions. They are very commonly found parallel to bedding planes in carbonates rocks. At both scales, pressure solution acts as a source of cement and an agent of compaction. It plays a significant role in porosity evolution and diagenetic compaction of rocks (Tada & Siever, 1989). Studies also suggest that pressure solution creep plays an important role in the strength and sliding behavior of faults, fault sealing, and, earthquake recurrence rates (Rutter & Mainprice, 1979 ; Bos et al., 2000 ; Hickman et al., 1995). The evidence for pressure solution in nature

is ubiquitous. Rocks from the upper to mid-crust in low metamorphic grade conditions exhibit clear evidence of fluid enhanced deformation: interpenetrating grains, stylolites, truncated fossils, tectonic overgrowths, striped cleavages, pressure shadows (Weyl, 1959 ; Trurnit, 1968 ; Rutter & Elliott, 1976 ; McClay, 1977 ; Tada & Siever, 1989). Quartz veins and slicken-fibers have been observed in exhumed faults (Durney & Ramsay, 1973 ; Cox & Paterson, 1991 ; Hickman et al., 1995).

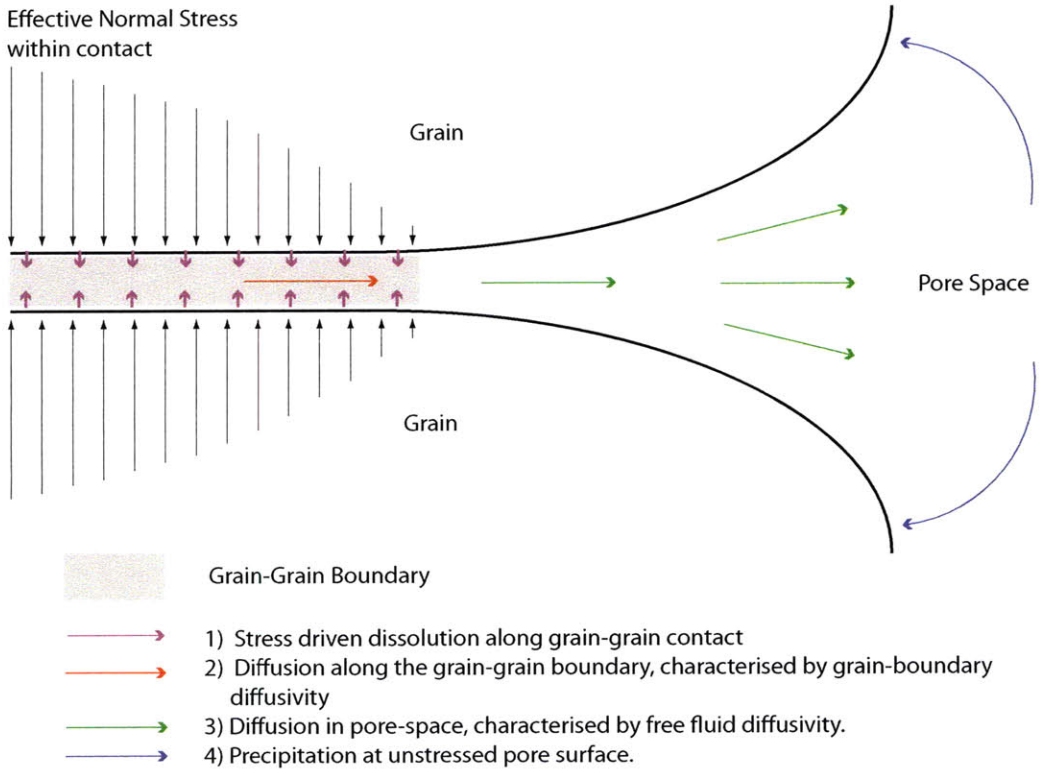

Figure 1-1: Illustration of pressure solution mechanism at a grain-grain contact

Pressure solution was first described by Sorby (1863) and became widely accepted after the systematic analysis of Stockdale (1926, 1936). Interest in pressure solution was renewed after the pioneering work of Weyl (1959). Paterson (1973), Rutter & Elliott (1976) and De Boer (1977) discussed the thermodynamics of pressure solution and attributed the driving force to the chemical potential difference between the stressed grain contact and relatively unstressed pore space. Later, Lehner (1985)

and Shimizu (1995) introduced non-equllibrium thermodynamics to the problem. Descriptions of mechanisms of pressure solution creep can be coarsely lumped into four different models: 1) fluid-film diffusion model, 2) island-channel model, 3) micro-cracking grain boundary model, and 4) under-cutting model.

Fluid-film diffusion model

The grain-grain boundary is assumed to be coated by a thin, structured, fluid film that supports the load and allows the material dissolved at the grain contacts to diffuse into the free pore space (Rutter & Elliott, 1976 ; Gratier & Guiguet, 1986 ; Hickman & Evans, 1995). The diffusivity in the film is often assumed to be less than that in a free fluid, but several orders greater than that in a dry grain-grain boundary. Diffusion through the grain-grain boundary is often assumed to be the rate-limiting mechanism in this model, which is adapted from the Coble creep law and has similar sensitivity to grain size and to stress. The volumetric strain rate is linearly proportional to the applied effective normal stress and inversely proportional to the cube of the grain size. Several experimental studies have appealed to this mechanism: Hickman & Evans (1995) monitored the evolution of the contact when a halite lens was pressed against fused silica. They concluded that diffusion is rate-limiting and estimated the film thickness to be less than 30 nm. Spiers et al. (1990) conducted compaction experiments on halite aggregates and concluded that diffusion is rate-limiting based on the observed grain size sensitivity. Experiments by Pashley (1981), Pashley & Israelachvili (1984) and Israelachvili (1986) suggest that such films can exist in silica, mica and alumina sheets. Nakashima (1995) found that the diffusivity of silica and oxygen ions in thin films is about $5 \times 10^{-14} m^2/s$ at room temperature and estimated the activation energy to be 15-30 kJ/mol. Despite these studies, the existence of the fluid film and the values of the diffusivity in the film and the thickness of the film are still debated. There is no clear experimental evidence of the existence of such films during pressure solution creep of quartzose rocks under natural hydrothermal conditions.

Island-channel model

Raj (1982) argued that fluid films cannot sustain shear stresses and proposed an island-channel structure that transmits the load through the islands and allows diffusion through the fluid in the channels. The diffusivity in the channels is assumed to be equal to the free fluid diffusivity and the interfacial kinetics (dissolution or precipitation) are considered to be rate limiting (Raj, 1982 ; Schutjens, 1991 ; Niemeijer et al., 2002 ; Noort, Spiers, & Pennock, 2008). The volumetric strain rate is inversely proportional to the grain size and linearly proportional to the effective normal stress. The stress sensitivity is linear only at low effective normal stress and exponential at higher stress (Niemeijer et al., 2002 ; Gratier et al., 2009). Raj assumed the island-channels to be non-equilibrium structures, dynamically maintained, owing to entropy creation. Noort (2008) attempted to justify the existence of island-channel structures and introduced a yield stress criterion above which island-channel structures exist and below which they heal. Many authors have identified micro-structures recovered after the experiments that resemble the island-channel structures (Cox & Paterson, 1991 ; Gratier et al., 2005). However, the origin is often ambiguous. For example, such structures can be formed by the healing of grain boundary fractures during unloading (see discussion in Hickman & Evans (1991)). Most of the experimental evidence (Schutjens, 1991 ; Niemeijer et al., 2002 ; Noort, Spiers, & Pennock, 2008) suggesting interfacial controlled pressure solution is based on estimation of a high activation energy (70-100 kJ/mol) and on micro-structure observations.

Micro-cracking grain boundary model

Gratz (1991) proposed a model that uses a hierarchical structure in which grain boundaries consist of islands coated by grain boundary films, separated by micro-cracks, and connected to inter-granular porosity. This model postulates that thin fluid-films exist at grain-grain contacts, but the diffusion rate along the thin films is not sufficient enough to cause geologically observed strain rates. Instead, the micro-cracks within the contact act as short-circuit paths for diffusion into the pore space,

enhancing deformation rates. Zubutsov (2005) conducted separate indenter experiments on halite and calcite at identical conditions and attributed the higher convergence rate in calcite, after correcting for difference in solubility, to the presence of micro-cracks beneath the indenter, in calcite.

Under-cutting model

In this model, the deformation is due to free surface dissolution at the edges of the contact and subsequent reduction in contact size leading to cataclastic failure (Bathurst, 1958 ; Weyl, 1959 ; Pharr & Ashby, 1981 ; Tada et al., 1987). This process is repeated, leading to time-dependent creep. Tada and Siever (1986) pressed a quartz knife against halite and observed under-cutting. On the other hand, Hickman & Evans (1995) did not observe undercutting in their halite-silica experiments. The under-cutting observed in Tada's experiment was due to the use of a sharp and rigid indenter that produces high stresses at the contact edges. Whereas, the contact geometries in Hickman & Evans (1995) experiments employed polished lenses, in which the highest stresses were in the center of the contact. Gratier's (2009) indenter experiments on quartz, using rectangular punch, also showed significant under-cutting, but grain boundary diffusion was identified as rate-limiting mechanism.

Pressure solution creep rates and the rate-limiting mechanisms are sensitive to the mineralogy of the solids in contact. Hickman & Evans (1991) did not observe pressure solution creep when a halite lens was pressed against halite. Rather, micro-structural evidence suggested healing of the grain boundary. They observed diffusion controlled pressure solution creep when halite was pressed against fused silica and a five fold increase in the convergence rates when a thin montmorillonite clay layer separated halite and silica (Hickman & Evans, 1995). This latter observation is consistent with the general observation from naturally deformed rocks and limited polycrystalline lab experiments that the presence of phyllosilicates enhances the pressure solution creep rates (Weyl, 1959 ; Rutter, 1983 ; Houseknecht & Hathon, 1987 ; Renard et al., 1997 ; Rutter & Wanten, 2000).

Though various authors argued whether dissolution or diffusion is rate-limiting,

it is possible that no single mechanism is rate-limiting at all the conditions and at all stages of the deformation process. Creep laws in the literature (Rutter & Elliott, 1976 ; Gratz, 1991 ; Niemeijer et al., 2002 ; Noort, Spiers, & Pennock, 2008) have, so far, simplified the problem by attributing average parameters to govern the creep law, assuming a single rate-limiting step under steady-state conditions. These models can be considered macroscopic. Lehner (1995) worked towards a microscopic model which considered several processes operating concurrently along the grain boundary. Recently, Bernabé and Evans (2007) proposed a numerical scheme to monitor the evolution of a single asperity due to pressure solution, accounting for the variability of properties along the grain boundary. Although Bernabé et al. did not make a priori assumptions about the distribution of stress along the contact, the numerical model considered only two of the many processes that might occur simultaneously in nature. Bernabé's simulations demonstrated that different processes are coupled and assuming a singe rate-limiting mechanism may not be correct.

1.2 Problem Statement

Despite considerable research on pressure solution, over the last few decades, the kinetics of the pressure solution process, identification of the rate-limiting mechanism and the nature of the inter-granular boundary during pressure solution (especially in quartzose rocks) is still not well understood. In this thesis, we focussed our attention on experimental studies of pressure solution creep at quartz-quartz grain contacts with controlled contact stresses and fluid chemistry and varied the structure at the contact to see the effect of morphology on pressure solution rates.

Chapter 2

Experimental Technique

2.1 Introduction

Experimental work on pressure solution (PS) creep often focuses on halite because significant strain rates can be achieved at relatively low temperatures ($8^0 - 90^0$C) and low effective normal stresses (1-14 MPa) (Hickman & Evans, 1995). For example, Tada and Siever (Tada & Siever, 1986) pressed a quartz knife against halite and noted that under-cutting is the dominant mechanism. Later, (Hickman & Evans, 1995) systematically studied PS at single grain-grain contacts between halite and fused silica, and established that diffusion is rate-limiting. Uniaxial compaction experiments by Spiers (1990) on halite aggregates also suggested that diffusion is rate-limiting.

In contrast, PS creep is slow in quartz and is active only at higher temperatures (above 350^0C) and higher effective normal stresses (Schutjens, 1991). The fastest strain rates estimated for minerals composed of quartz deforming via PS in nature are of the order of 10^{-11}/s (Rutter & Elliott, 1976) and observing such slow rates experimentally is hard. Creep in the lab can be artificially expedited by using a alkaline solution (De Boer, 1977 ; Gratier & Guiguet, 1986) or working at higher temperatures (Cox & Paterson, 1991 ; Luan & Paterson, 1992) or at high normal stresses (Gratier et al., 2009), each having its own side effects. In a very different type of experiment, Sprunt and Nur (1977) demonstrated the stress dependence of solution transfer in quartz at a free-face subjected only to in-plane tangential stress, by loading quartz

slab containing a hole, under uniaxial compression perpendicular to the hole axis. They concluded that dissolution was rate limiting in this case of "free-face" pressure solution. De Boer (1977) compacted quartz aggregates uni-axially in a brine medium (360^0C; 51 MPa effective pressure) and showed micro-structural evidence for pressure solution. Gratier & Guiguet (1986) showed that the compaction rates increase with the concentration of NaOH in pore fluid and are inversely proportional to the grain size. He reported dissolution to be the rate-limiting step. Cox & Paterson (1991) conducted compaction experiments on quartz aggregates at elevated temperatures (1200^0 K, 100 MPa effective pressure) and observed relatively high strain rates (10^{-6}/s). They interpreted the micro-structures to resemble island-channel structure and argued that interfacial kinetics were rate-limiting. Schutjens (1991) performed 1D compaction tests on quartz sands ($150-300^0$C, 20.7 effective pressure, 20-100 μm grain size) and observed strain rates of $10^{-8}/s$. He reported an activation energy of 61-76 kJ/mol and wide-spread micro-cracking in the recovered micro-structures. He suggested that deformation is controlled by time-dependent micro-cracking below 300^0C and interface-limited pressure solution above 300^0C. Dewers & Hajash (1995) isostatically compacted aeolian quartz sand ($150-200^0$C, 35 MPa effective pressure) and inferred that PS was the dominant mechanism, but was accompanied by time-dependent cataclasis at lower temperatures. Based on the activation energy (73 kJ/mol), Dewers & Hajash (1995) concluded that interfacial kinetics was rate-limiting. The influence of clay on pressure solution rates in quartzose rocks was tested by a few authors. Rutter & Wanten (2000) observed an increase in compaction rates in phyllosilicate bearing sands (300^0-450^0C; 10-210 MPa effective pressure). However, Niemeijer (2002) did not observe any enhancement in creep rates when muscovite was added to the quartz aggregates, under similar conditions (500^0C; 100 MPa effective pressure). The influence of clays has to be explored further. When not mentioned explicitly, the pore fluid was pure water in the above experiments.

Niemeijer (2002) studied pressure solution creep in quartz aggregates more systematically. He conducted isostatic compaction experiments on quartz aggregates, varying the temperature (400^0-600^0C), effective pressure (50-150 MPa) and grain

size (30-100μ m). He reported an activation energy of 77.6 kJ/mol, stress exponent of 3 and an inverse grain size dependence. Comparing these results with interface-controlled pressure solution rate laws and based upon his observed activation energy, he concluded that dissolution was rate-limiting. Noort (2008) arrived at the same conclusions from his isostatic compaction experiments on quartz aggregates (3-129μm initial grain size, $300^0 - 600^0$C, 25-100 MPa effective pressure), but also, noted that micro-structures were dominated by micro-fracturing at low temperatures, giving way to pressure solution related micro-structures at higher temperatures. Karner (2003) and Chester (2004 ; 2007) monitored the acoustic emissions during compaction experiments on quartz aggregates at low temperatures ($25^0 - 150^0$C). The cumulative number of acoustic emissions scaled with total volumetric strain and strongly suggest micro-cracking and frictional grain sliding. Though these experiments were conducted at relatively low temperatures, the results emphasize the role of cataclasis in aggregate experiments. He (2007) reported that micro-granulation at quartz grain boundaries resulted in production of high energy ultra-fine particles that enhanced dissolution (150^0C; 34.5 MPa effective pressure).

Most data from aggregate compaction experiments in quartz suggest that interface kinetics are rate-limiting. But, most workers arrive at this conclusion by comparing their measured apparent activation energy (about 60-100 kJ/mol) with that for dissolution in quartz (61-105 kJ/mol) (Rimstidt & Barnes, 1980). However, these activation energies are comparable to the activation energy of sub-critical crack growth (Atkinson, 1984) and so, it is not straight forward to distinguish between the two mechanisms. In addition, it is likely that multiple mechanisms operate in the aggregate compaction experiments, complicating the interpretation of mechanical data.The complicated mechanisms present in the aggregate experiments suggest that simpler experiments with more controlled geometries might be useful. Indenter techniques offer simple geometries to study the problem.

Recently, Gratier (2009) published his work on indenter experiments on quartz, spanning a 10 year period. He pressed a steel indenter (200μm diameter) against a quartz single crystal in NaOH solution at 350^0C and under differential stress (uniax-

ial stress - pore fluid pressure) varying from 25-350 MPa. He varied the orientation of the pressed surface, the NaOH concentration in the pore fluid and the nature of quartz (natural or synthetic). Unfortunately, he could not vary the indenter diameter and thus could not test the grain size sensitivity. In general, he observed more indentation rate with increasing NaOH concentration and an exponential dependence of indentation on differential stress. Based on the growth kinetics of different faces of quartz and comparing the observed strain rates with diffusion and dissolution controlled rate laws, he concluded that diffusion was rate-limiting. However, due to the flat-bottomed geometry of the indenter, there was considerable free-face dissolution and "en echelon" fractures formed around the indenter. In addition, his experiments involved interfaces (quartz-steel) which probably alter the kinetics (as observed for halite/silica contacts (Hickman & Evans, 1991)). It is, thus, desirable to study single quartz-quartz contacts, to allow for a more direct comparison with mono-minerallic quartz aggregates deformed in nature and in the laboratory.

In this study, we monitored pressure solution at single quartz-quartz grain contacts by pressing a quartz plano-convex lens against a quartz plano-plano lens under hydrothermal conditions (425^0C, 150 MPa fluid pressure), using dead quartz weights. This well-defined geometry allows us to estimate the stress field within the contact, to have control over diffusional path length and to monitor convergence and contact evolution in real time. In addition, this configuration does not induce high stress concentration at the contact edge, a situation which leads to free-face dissolution (Gratier et al., 2009). The experimental technique is very similar to that used by Hickman & Evans (1991, 1995). The mutual approach of the lenses is measured using optical interferometry, accurate to 0.02μm.

The objective of the experiments was to see if quartz-quartz contacts healed or deformed at hydrothermal conditions and to examine the effect of boundary morphology on the pressure solution creep rates.

2.2 Sample Preparation

The plano-convex lenses and the plano-plano lenses (referred to as quartz flats, or simply, flats) used in the experiments were Y-cut single crystals of synthetic alpha-quartz. The radius of curvature of the plano-convex lenses was 0.443 inch. The quartz flats were 0.7 inch in diameter and 0.25 inch in thickness. The lenses and flats were prepared and polished by *Boston Piezo-Optics*, Bellingham, MA, from the quartz crystals synthesized by *Sawyer Research Products*, Eastlake, OH.

As mentioned earlier, our goal was to examine the effect of surface morphology on PS rates. We used a smooth quartz flat in our first experiment, PS031209, as a control and then introduced more complicated surface structures in the later experiments. Some trial and error was necessary to achieve repeatable, well-characterized surface morphologies. We first attempted to fabricate an inter-connected grid of channels on the surface of the quartz flat by wet etching with 49% HF acid. A fine Ni wire mesh (2000 wires per inch, each wire 5μm thick) was laid over the flat surface of the quartz flat (sample 5) and gold was vapor deposited over it. Then, the Ni mesh was carefully removed leaving the surface exposed in a gridded pattern of straight lines matching the mesh pattern and size. The gold coating masked the remaining surface. The surface of the flat with the pattern on it was exposed to HF vapors by holding the surface at a distance 3mm away from 49% HF solution at 60^0C for 3.5 hrs. The etch rate was approximately $0.286\mu m/hr$ in a direction normal to the surface. We expected the exposed area to be etched, leaving a grid pattern of inter-connected channels with their depth proportional to the exposure time. But, the gold pattern was washed away and the surface exhibited anisotropy in the etch rates along different crystal directions. This resulted in triangular etch pits of comparable size all over the surface, with no grid pattern evident. Nevertheless, owing to the overall roughness of the surface produced, these features could have produced the desired effect: produce stress concentrations within the contact and provide short-circuit pathways for diffusive transport. We characterized the etched surface using a mechanical probe profiler, *Talyscan 150*. The etch pits were, on an average, 1$\pm$0.2μm

deep. This quartz flat (Sample 5) was used in the experiment PS041309.

To avoid anisotropy in the structure introduced by wet-etching, we next tried dry/plasma etching. The plasma is generated on ionizing the etchant gases in vacuum by using RF excitations. Because the plasma etch process uses a large energy, the effects of differences in the surface energy along different crystal directions on etching rates is negligible and do not cause anisotropic etching. Since plasma etches both the mask and the substrate, the plasma should be designed to selectively etch the substrate (here quartz). Ideally, we want the plasma to etch normal to the surface without undercutting the mask. The gases in the plasma and their ratio determine the selectivity of the process and the etch rates normal and parallel to the exposed surface. The masking material should adhere well to the surface, be resistant to the etching plasma, but be removed easily by a chemical treatment neutral to the substrate. We used *Drytek4*, an inductively coupled plasma etching machine, at Stanford Nano Fabrication Facility (SNF) to plasma /dry etch the quartz flats. The plasma etchant was a gaseous mixture of CHF_3 (100 standard cubic centimeters per minute , sccm) and O_2 (10 sccm) ejected from an Al ionizing electrode. *Drytek4* was operated at 150 mT (milli Torr) pressure, 150W power and 310-330V voltage. Chromuim(Cr) was chosen to be the masking material due to its good adhering property to oxides and low etch plasma rate. Standard Cr etchant (22% Ceric Ammonium Nitrate, 9% Acetic Acid, 69% water) was used to remove the Cr masking layer on top of the quartz flat after dry/plasma etching. The etch rate, normal to the surface, was observed to be approximately $1.2\mu m/hr$.

The structure on 'Sample 2' was fabricated by dry/plasma etching as follows: A Ni mesh (1500 wires per inch, each wire 5.6μm thick) was laid on the flat surface of the quartz flat. The mesh was carefully removed after Cr deposition to leave a grid pattern of lines (approximately as wide as the thickness of the wires) as discussed earlier, while the rest of the surface was masked by Cr. This surface was then subjected to plasma etching. Quartz was etched all along the grid pattern of lines leaving interconnected channels on the surface. The residual Cr, masking the space in between the channels, was removed by wet etching the sample with standard Cr etchant. Thus, we

fabricated an island-channel structure of square pillars surrounded by interconnected grid of channels. The etched surface of the flat was characterised using *Zygo White-Light 3D Surface Profiler*, which is based on optical phase-shifting interferometry. In plan view, the top surfaces were slightly rounded (Figure 2-1(a)). The height of the pillars or the depth of the channels was $1.05\pm0.005\mu$m and the channels were trapezoidal in cross section (Figure 2-2(a)). The average dimensions of the pillars and channels are tabulated in Table B.1.'Sample 2' was used in experiment PS052009.

The plasma etching protocol was successful, but it was difficult to control the masking process when we used the Ni Mesh. Moreover, the width of the channels was limited by the Ni wire thickness. So, optical photolithography, a standard procedure in semi-conductor manufacturing, was used to make the patterned Cr mask on subsequent samples. This method involves creating a pattern on photo-resist, a photosensitive material, by exposing it to light through a photo-mask, that carries the pattern, through the following process. First, the quartz flat was coated uniformly with Cr (thickness $\approx$840 A^0). A photo-resist was spun onto the Cr layer and then exposed to a pattern of grid of lines, using the photo-mask. The resist was then developed, uncovering the Cr layer beneath the pattern. The flat was then treated with standard Cr etchant, exposing the quartz surface through the grid pattern. The photo-resist on top of the remaining Cr layer was stripped to leave the sample with a Cr mask. The entire process is explained in detail in Appendix A. During exposure, we aligned the crystallographic c-axis of the quartz flats with the grid pattern on the photo-mask.

Using this photo-lithography process, we fabricated a 4μm wide, 0.5μm deep interconnected grid of channels spaced 8μm center to center on four flats (Samples b2, c1, a1 and d) by etching the samples with plasma for 24 minutes. Similarly, we fabricated an 8μm wide, 1μm deep interconnected grid of channels spaced 16μm center to center on four flats (Samples 2, b1, c2 and a2). These samples were plasma etched for 48 minutes. The etched surfaces of all these flats were characterised by *Zygo White-Light 3D Surface Profiler*. The actual dimensions of the fabricated structures were very close to the attempted values and are tabulated in Table B.1.

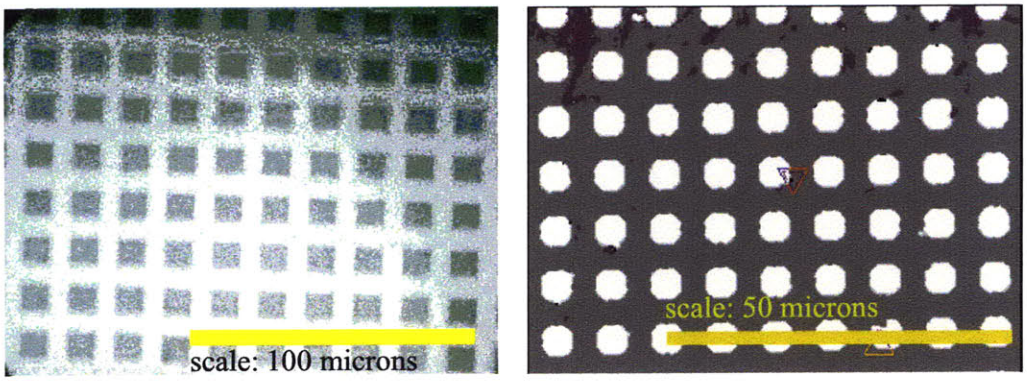

(a) Sample 2 (b) Sample c1

Figure 2-1: Plan view of the fabricated island-channel structures

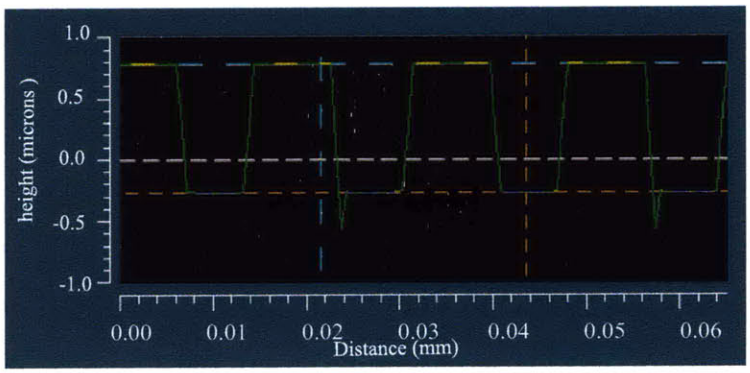

(a) Sample 2

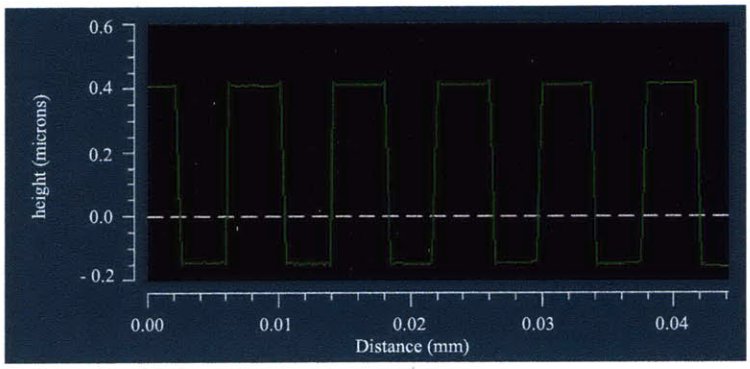

(b) Sample c1

Figure 2-2: Profile through the center of pillars along the grid, on (a) 'Sample 2' (b) 'Sample c1'

'Sample c1' was used in experiment PS062309. A plan view of the fabricated island channel structure on 'Sample c1', as measured by *Zygo*, is shown in Figure 2-1(b). A cross section along the centers of pillars is shown in Figure 2-2(b). The depth of the channels or the height of the pillars was $0.55 \pm 0.005 \mu$m. The dimensions of the surface structure are tabulated in Table B.1. The fabricated island-channel structures on 'Sample 2' and 'Sample c1' were oriented at an angle of 5^0 from the crystallographic c-axis despite our efforts to align them during fabrication.

2.3 Experimental Set-up

To measure the evolution of the quartz-quartz contacts, we pressed the convex side of the plano-convex quartz lens against a plano-plano quartz flat under hydrothermal conditions in a see-through optical pressure vessel. A constant normal load was applied throughout the duration of the experiment (2-3 weeks) by means of quartz dead weights. The weights also served to maintain the fluid at maximum concentration of silica in experimental conditions. A schematic diagram of the apparatus is shown in Figure 2-3.

The pressure vessel (Beeler & Hickman, 2004) is an externally heated pressure vessel made up of Rene 41 (Inconel), with valves for inlet and outlet of fluid on the top and a cone-in-cone seal utilizing an Inconel seal at the bottom. We controlled the fluid pressure in the vessel, using a hydraulic pump, an inline pressure transducer, and a pressure gauge accurate to ± 2 bars. A detachable three-coil furnace was used to maintain uniform temperature throughout the vessel. Thermocouples (accurate to $\pm 0.2^0$C) were attached to the inner metal sleeve on which the three coils of the furnace were wound and provided input to three Omega furnace controllers that controlled input current to the coils. The temperature at the contact was monitored by a thermocouple inserted into a hole bored into the pressure vessel that was close to the samples. Furnace profiling conducted earlier shows that the actual temperature at the contact is within 10^0C of the measured value. The interior of the vessel was lined with gold to prevent corrosion and to control the fluid chemistry.

Inside the pressure vessel, the quartz weights were stacked on top of the quartz lenses, and were held in a coaxial position by a gold wire passing through a hole in the center of the cylindrical weights (Figure 2-4). The load was transferred onto the flat surface of the lens through the spherical tip at the end of the gold wire. This pressed the curved surface of the lens against the quartz flat, which sat over the observation sapphire window. The flat and the window were separated by a thin annular gold ring to avoid interference of light reflected from the bottom of quartz flat and the top of sapphire window. The sapphire window rested on a polished annular flat at the top of the conical seal with an intervening annealed gold washer, which deformed as the fluid pressure was increased and sealed the vessel. Figure 2-4 shows a schematic diagram of the lens geometry inside the pressure vessel and the loading mechanism.

A long working-distance microscope was equipped with a digital camera to monitor the evolution of the contact as the experiment proceeded (Figure 2-3). A mercury-zenon arc lamp in conjunction with a grating monocrometer was used as a tunable monochromatic light source, which operated over a range of wavelengths (360 nm to 600 nm). An 'AVT PIKE F-100 B' camera, operated at 60 fps and 1 mega pixel resolution, was used to take the photomicrographs in all the experiments, except the experiment PS031209, which used an older, analog camera and frame grabber card. The vessel and the optical equipment were placed on an air-suspension vibration isolation table during the experiment.

The quartz weights, lenses, sapphire window, gold ring, gold washer, gold wire and the conical seal of the vessel were cleaned with acetone, methanol and de-ionised water in an ultrasonic cleaner before assembly. The interior of the pressure vessel was also rinsed with acetone, methanol and de-ionised water. While assembling the pressure vessel, we first inserted the sample assembly and weights, filled the vessel with de-ionised water, sealed it and raised the confining pressure. The contact between the lenses was fully saturated with de-ionised water. After the vessel was pressurized (about 50 MPa), the furnace was lowered over the pressure vessel and the temperature was raised slowly from room temperature (22^0C) to the target temperature, while the pressure was manually controlled to achieve its final desired value.

This process was slow enough (about 4 hours) that the de-ionised water should have reached silica saturation by the time it reached run conditions through dissolution of the quartz weights (see discussion in Beeler & Hickman (2004)). The design pressure and temperature were 150 MPa and 425^0C, respectively and were continuously recorded during each experiment. The pressure was maintained at 150 ± 1 MPa. The temperature in the vessel, as measured by the thermocouple in the lower seal of the vessel, varied from experiment to experiment from 414^0C to 418^0C. During a single experiment temperature fluctuated by $\pm1^0$C.

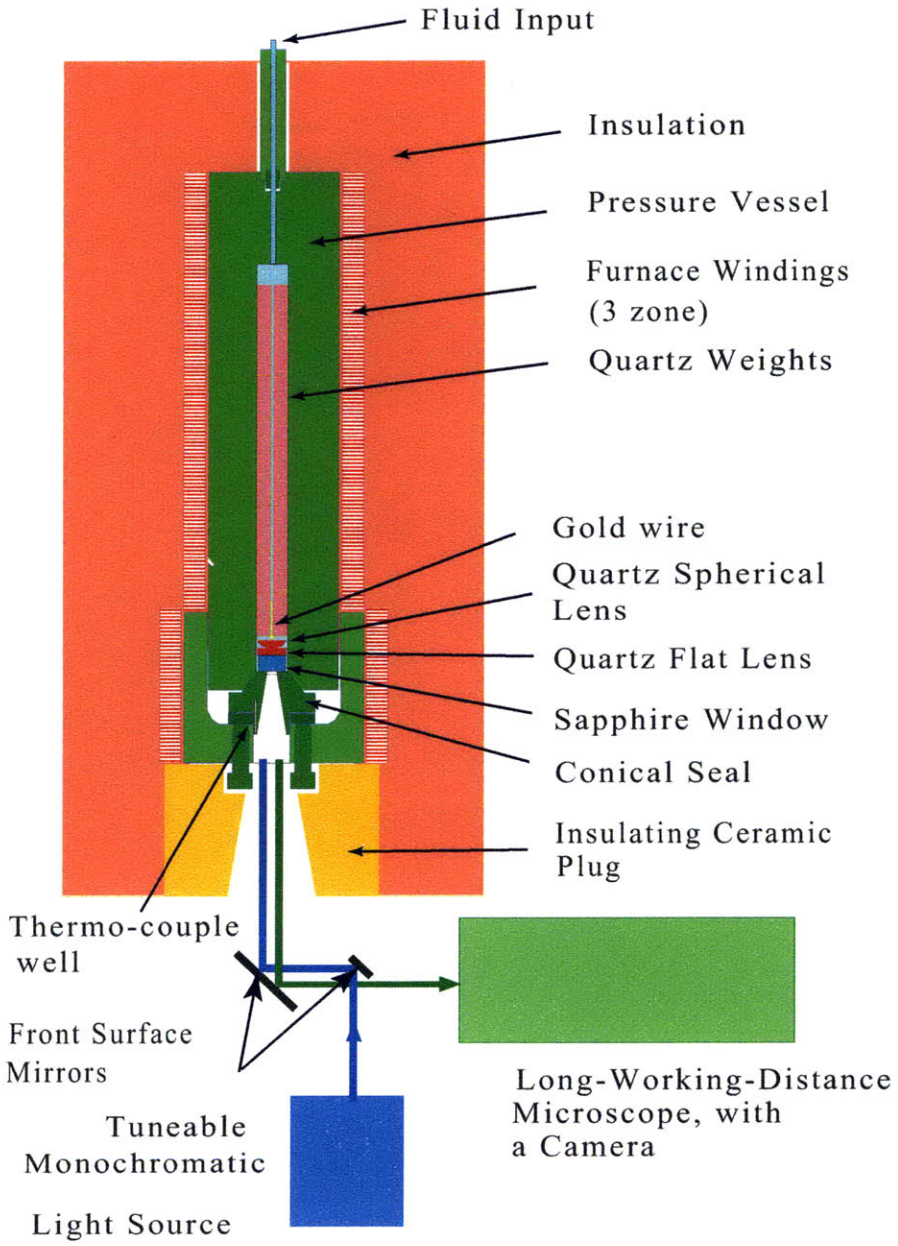

Figure 2-3: Schematic diagram of the experimental set-up

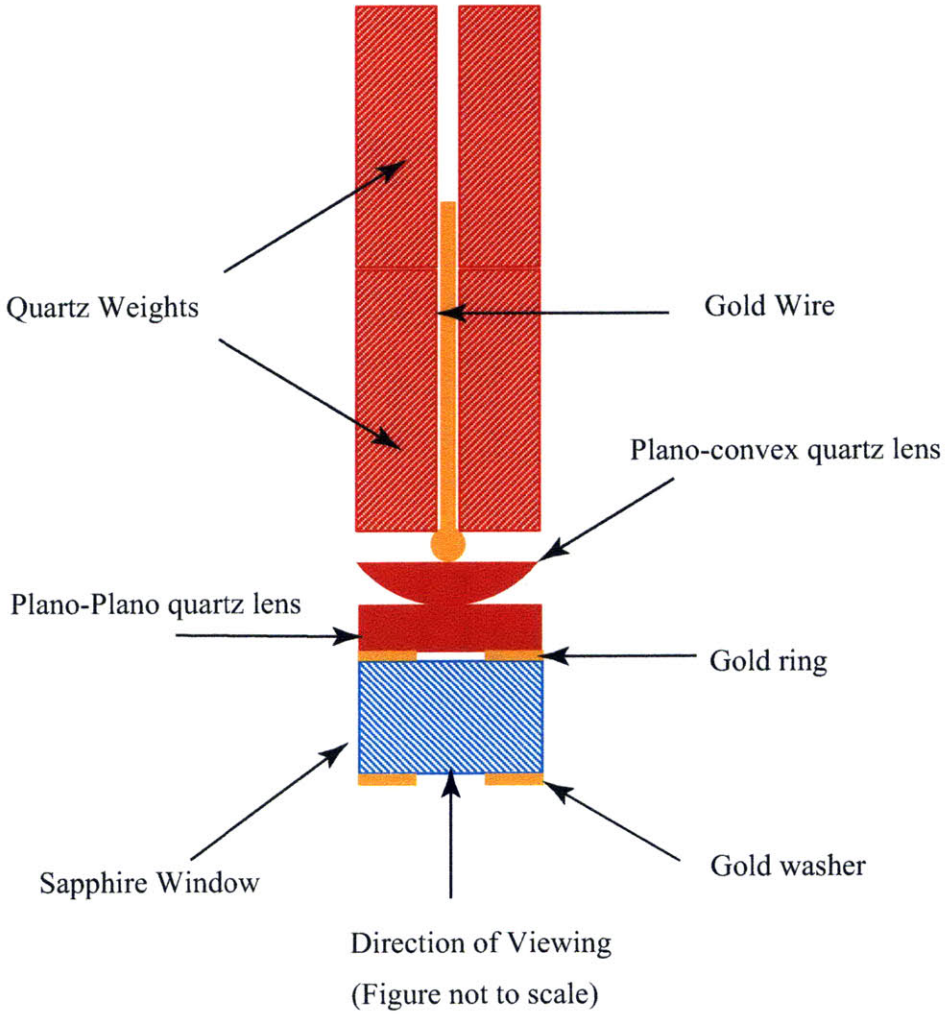

Figure 2-4: Schematic diagram of the lens geometry inside the pressure vessel

Chapter 3

Analysis

3.1 Convergence Measurement

Convergence is defined as the relative approach of two distant reference points in the two lenses when they are pressed against each other, under the experimental conditions. When the load is applied, we expect an instantaneous convergence due to the initial elastic/plastic deformation. Creep mechanisms lead to a time-dependent convergence. Convergence is measured using the move-out of the interference minima in the Newton's rings pattern (Hickman & Evans, 1991, 1995). For example, in Hickman & Evan's (1991) halite-halite pressure solution experiments, neck growth occurred without convergence. The contact size (the central dark spot) increased without any move-out in the interference pattern.

The light rays reflected back from the bottom of the convex lens and from the top of the flat interfere constructively or destructively depending upon the thickness of the fluid layer between the two surfaces. Thus, we see a pattern of concentric bright and dark bands corresponding to the interference maxima and minima. As the lenses move towards each other, the separation between the lenses decreases and the rings appear to move out from the center. By tracking the change in the radius of the interference minima, convergence is measured. The separation between the lenses required for minima is given by:

$$h_m = \frac{m\lambda}{2\mu}, m = 0, 1, 2, 3, .. \tag{3.1}$$

where m is the order of the interference minima, λ is the wavelength used for observation (here we used 435 nm, 542 nm and 575 nm) and μ is the refractive index (see section 3.5) of the saturated quartz solution.

As explained above, the position of the interference minima is a function of the thickness of quartz solution separating the lenses. The thickness of the quartz solution, between the lenses, 'h', at a radial distance r from the center of the contact is given by (see figure 3-1):

$$\begin{aligned} h(r) &= R_c - s - \sqrt{R_c^2 - r^2} \approx \frac{r^2}{2R_c} - s \\ &= \frac{r^2}{2R_c} - s \qquad \text{from binomial expansion,since } R_c >> \text{r} \end{aligned} \tag{3.2}$$

where, R_c is the radius of curvature of the lens (0.443 inch), s is the total convergence until the time of observation. For the case, when we have pillars on top of the quartz flat and 'h' is measured relative to the base of the pillars,

$$h(r) = \frac{r^2}{2R_c} + h_0 - s \tag{3.3}$$

where h_0 is the height of the pillars (see Figure 3-1). Combining equations 3.1and 3.3,

$$s = \frac{{r_m}^2}{2R_c} + h_0 - \frac{m\lambda}{2\mu} \tag{3.4}$$

Since, we are interested only in the time-dependent deformation at the contact, we look for the time dependent component of convergence after the initial elastic/plastic loading. From equation 3.4, Δs = s(t)-s(0), is given by:

$$\Delta s = \frac{\Delta {r_m}^2}{2R_c} \tag{3.5}$$

where $\Delta {r_m}^2$ is the change in the square of the m^{th} order fringe radius relative to its value just after loading.

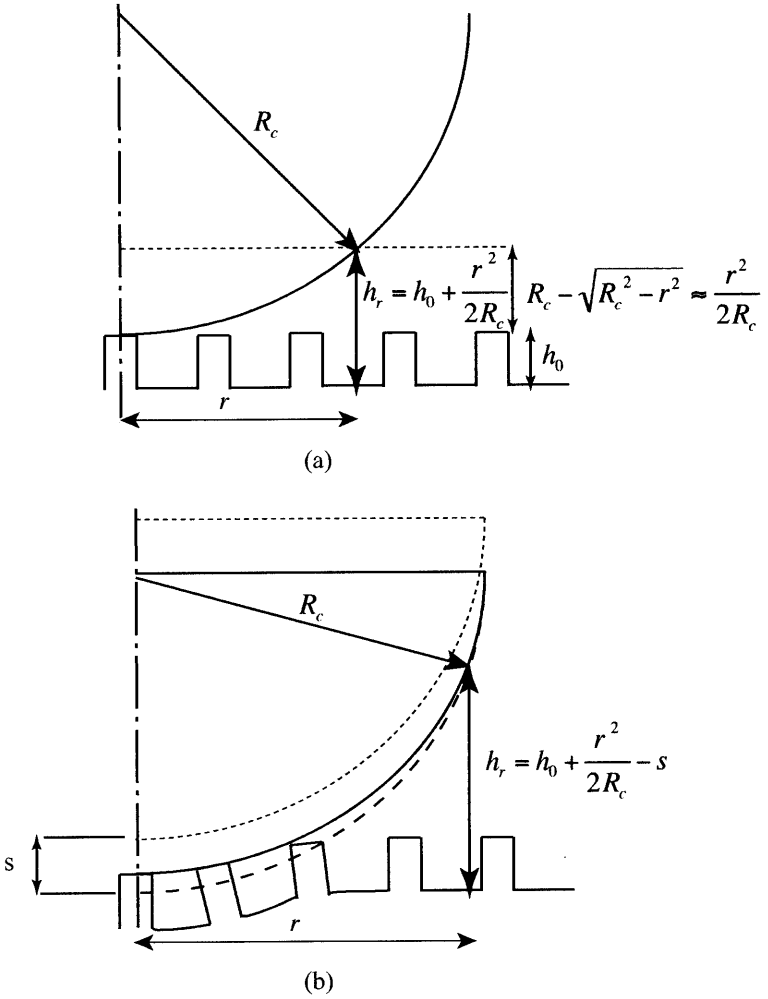

(a) : Separation between the lenses when no load is applied.

(b) : Separation between the lens when they are pressed against each other. The profiles come closer by the total convergence 's'

R_c Radius of Curvature of the Convex lens

h_r Thickness of the quartz solution between the lenses at a radial distance 'r'

h_0 Height of the pillars above the flat lens

Figure 3-1: Schematic diagram of profile separation

Knowing the radius of curvature of the lenses, we determined Δs by measuring the change in the radius of the interference fringes. The radius of the interference fringes were measured as described in section 3.2. The convergence was calculated using the equation 3.5 for each tracked interference fringe and averaged, using calculations of refractive index to identify the order of each fringe (see sections 3.5, 3.6). The standard deviation of the convergence value was less than the estimated error in the convergence (see section 3.2). We ignored the first few fringes, which tend to be distorted, and tracked up to 8 - 10 fringes in each interferogram.

3.2 Radius of Interference Minima

The radius of each interference minimum was tracked in the time-lapse photos of the contact. The accuracy with which we can measure the radius is theoretically limited by the resolution of the photo. In addition, the illumination was not uniform, introducing extra noise in the experiments. We processed the images by rescaling the color histograms to enhance contrast. We applied a band-pass filter, to enhance features greater than 4 pixels and smaller than 40 pixels, which reduced the spatial variation in brightness due to non-uniform illumination and also suppressed the high frequency noise. The processed photos were finally analyzed to measure the radius of the interference minima.

The radius of each interference minima was calculated separately through a two-step process. First, a minimum of 10 points was selected manually on each interference fringe. The best-fit circle to the manually selected points was determined by non-linear least squares. The best-fit circle was then discretized. At each point on the discretized circle, a square region of pixels, with the discretized point at the centre, was selected. The side of the square was approximately equal to the width of the fringe. The weighted centroid of the square region was calculated, with the pixels weighed exponentially by darkness. This centroid was assumed to represent the minimum of the considered fringe. The radius of the best-fit circle to these centroids was taken to be the radius of the interference minimum. The root mean square error in

the radius of the best-fit circle, thus calculated, varied from 0.5 pixels to 1.5 pixels. Thus, the radii of interference minima were estimated within $\pm 1.5\mu$m.

The non-linear least squares algorithm, used to find the best-fit circle, iteratively solves for the center of the best-fit circle. The radius of the best-fit circle is the average radial distance of the data points from the center. The algorithm minimizes the l_2 norm of the difference between the radial distance of each point and the average radial distance of all points. The initial guess to the non-linear least squares algorithm was the average of the centers of circles, passing through three points selected at a time. Points too close to each other were avoided. The termination criteria were the default termination criteria of Matlab optimization toolbox.

Propagating the error in the measurement of radius into convergence calculations, the error in measuring the convergence, Δs_{error}, is of the order of 0.02μm on average (see Figure 4-2(b)). Thus, we can measure convergence accurate to 0.02μm.

3.3 Newton's Rings Pattern

When we used quartz flats with added surface morphology the interference pattern was complicated (see Figures 4-3, 4-4, 4-5 and 4-6). In particular, in the case of square pillars, the central interference pattern appears to be surrounded by additional interference patterns (see Figures 4-5 and 4-6), which are caused by the interference of rays reflected from either the top of the pillars or the bottom of channels with rays reflected from the bottom of the convex lens. However, if the pillars and channels occupy different surface area, the interference pattern corresponding to the greatest surface area dominates. For example, if the channels occupy more surface area than the pillars, the interference pattern associated with the bottom of the channels will dominate.

To interpret the observed interference pattern, we numerically modeled the interference pattern due to a convex lens on top of a flat with pillars as follows. The center of the lens is assumed to rest on the center of a pillar and the separation between the two lenses at any point on the surface of the flat is calculated. Whenever the point

lies on top of a pillar the separation 'h' is given by the equation 3.3, depending on the radial location of the point from the axis of symmetry of the convex lens. Similarly, whenever the point lies on the bottom of a channel, the separation is given by the equation 3.2, depending on the radial location of the point. The phase difference between the rays reflected from the bottom of the convex lens and the top of the quartz flat, ϕ, is given by

$$\phi = 2\mu h \frac{2\pi}{\lambda} + \pi \tag{3.6}$$

The extra phase difference of π is introduced by the reflection at the bottom of the convex lens due to reflection at medium with higher refractive index. For the purpose of calculating the position of the minima and maxima, we assume total reflection and thus, both the interfering wave fields have same amplitude,ψ_0. The resultant amplitude at any observation point ψ is given by :

$$\psi = \psi_0 \sqrt{2\,(1 + \cos(\phi))} \tag{3.7}$$

This assumption only affects the amplitude values at the observation points, but not the position of the minima and maxima. A numerically computed interference pattern is compared with the observed interference pattern when the convex lens was pressed onto 'Sample 2' at a load of 0.015 N in air (Figure 3-2). The separation between the lenses for use in the simulation was calculated using equations 3.2, 3.3, assuming an elastic initial convergence (see section 3.6). Note that the concentric bands surrounding the central interference pattern, as well as the overall intensity of the central contact spot in the simulated pattern matches the observed pattern quite well. This good agreement indicates that the central interference pattern observed with 'Sample 2' (Figure 3-2(a)) is formed on the bottom of the channels. This can also be seen in Figure 3-3, which shows the interference patterns when either channels or pillars occupy more surface area. We can see that a bright central interference pattern is formed only when more light is reflected off the bottom of the channels (Figure 3-3(a)).

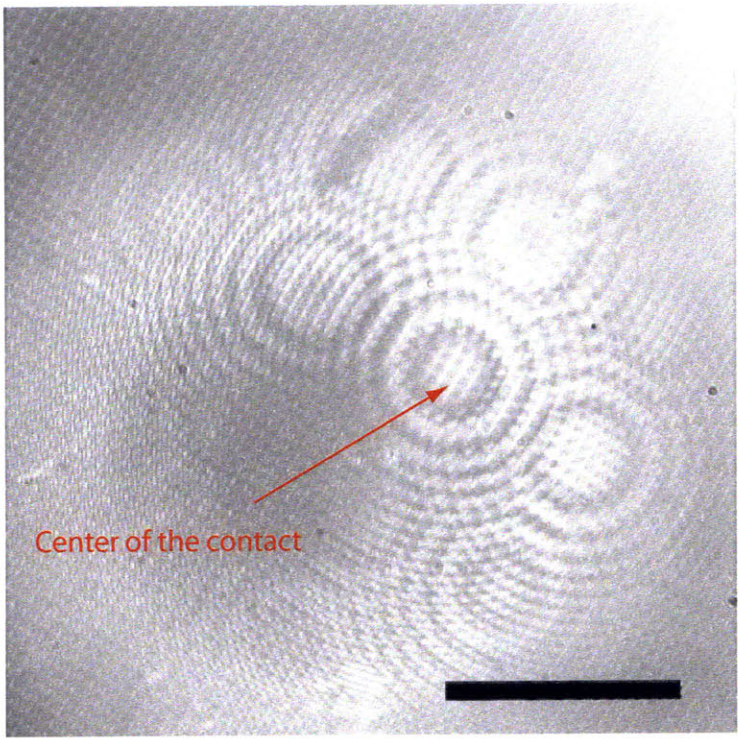

(a) Observed Pattern

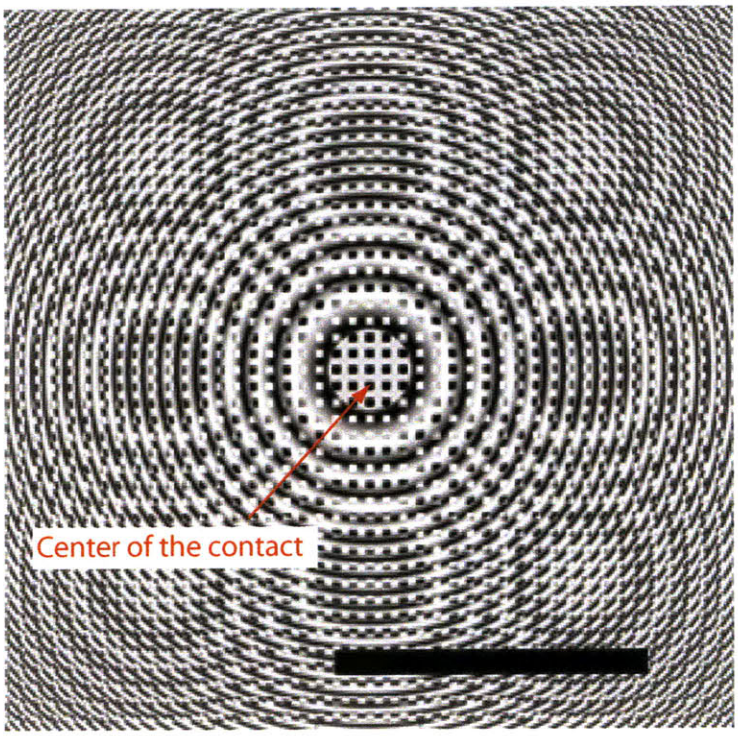

(b) Simulated Pattern

Figure 3-2: Comparison of observed and simulated interference patterns. Scale bar is 300 microns

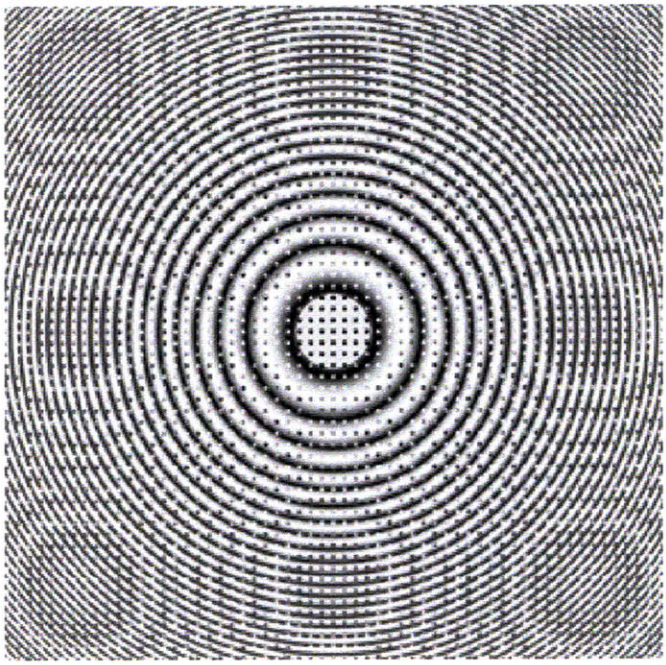

(a)

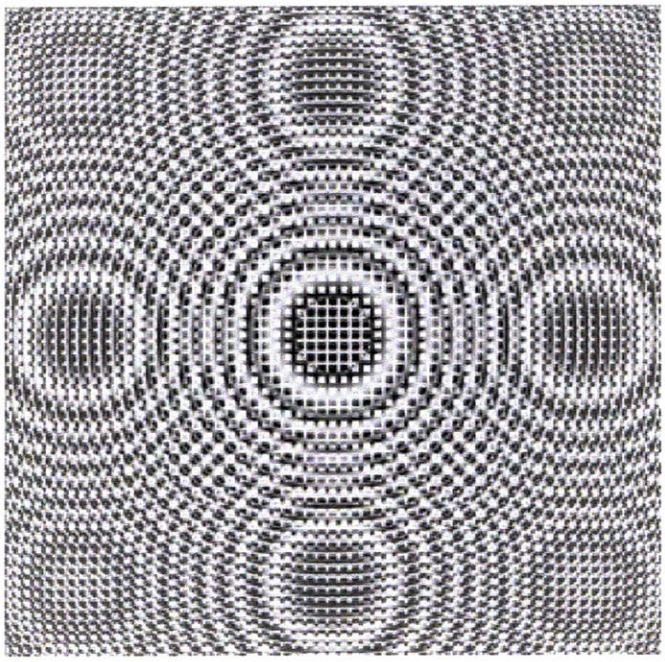

(b)

Figure 3-3: (a) Channels occupy more surface area: Interference pattern is on the bottom of channels (b) Pillars occupy more surface area: Interference pattern is on the top of Pillars

3.4 Stress Estimation

From Hertzian Contact theory, we estimate the contact stresses in our experiments by calculating the stress distribution produced by the contact of a sphere pressed against a flat (Johnson, 1985). This is readily applicable to experiment PS031209, where no morphology was added to the surface. But, the stress distribution within the contact is more complicated with experiments PS052009, PS062309. We estimate the stress distribution within these contacts by considering the fabricated pillars as rigid punches. Indeed, the elastic shortening of the pillars (about 0.01 μm for a mean stress of 1000 MPa on the pillars) is small compared to the overall elastic displacement (about 0.26 μm for a load of 0.85 N). In these calculations, we assume a square grid of pillars with the center of the contact located on top of a central pillar (eg: Figure 3-1). In this configuration, we have rings of pillars located radially from the center of lens (see Figure 3-4). For a contact problem, we need to solve for both contact radius and the stress distribution. We do it iteratively, as follows: 1) First, the contact radius / the number of rings in contact is guessed. 2) The load distribution on the pillars within the contact is computed (as explained below). 3) The contact radius (thus, the number of rings in contact) is increased if all the pillars within the contact are under compression. The contact radius is decreased if any pillar within the contact is under tension. 4) Steps 2 and 3 are repeated until the number of rings in contact is maximized when all the pillars within the contact are under compression. The deformation in the lens and the flat (which is assumed identical) is calculated from the distributed loads exerted by the pillars within the contact.

At a given iteration, let the rings i = 0 to m be in contact. The zeroth ring corresponds to the central pillar while the m^{th} ring corresponds to the outermost ring in contact. The number of pillars on the i^{th} ring (radius r_i) is given by n_i. For a given macroscopic load 'P' on the lens, we assume that all the pillars on a ring share the same load p_i (from symmetry arguments). Following Hertz's approach to contact

problem, the following conditions are true for pillars inside and outside the contact:

$$\begin{aligned} h_i &= 2u_0 - 2u_i \qquad i \leq m, \text{ inside the contact} \\ &> 2u_0 - 2u_i \qquad i > m, \text{ outside the contact} \end{aligned} \tag{3.8}$$

where h_i is the separation between pillars on the i^{th} ring and the lens, given by $\frac{r_i^2}{2R_c}$, u_0 is the normal displacement under the central pillar, and u_i is the normal displacement under the pillars on the i^{th} ring, caused by the elastic deformation of the surface of the flat. $2u_0$ is the relative approach of two distant points in the lens and the flat.

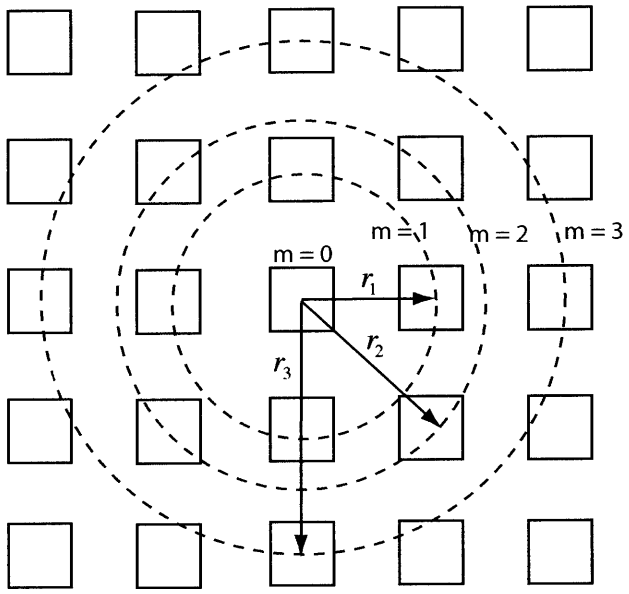

Figure 3-4: Illustration of pillars within the contact

An expression for the normal displacement, 'u_i' is obtained by considering the displacement under a given pillar due to the load on all the pillars in contact. The normal displacement 'u' at a radial distance 'r' from the center of the punch (here representing a pillar), due to a load 'P' on it is given by (Johnson, 1985):

$$\begin{aligned} u &= \frac{(1-\nu^2)P}{2Ea_p} \qquad \text{for } r \leq a_p, \qquad \text{i.e, beneath the punch} \\ &= \frac{(1-\nu^2)P}{\pi E a_p} \arcsin(\frac{a_p}{r}) \qquad \text{for } r > a_p, \qquad \text{outside the punch} \end{aligned} \tag{3.9}$$

For a given pillar on the i^{th} ring (i=0,1,2,..., m), u_i is given by:

$$u_i = \frac{(1-\nu^2)p_i}{2Ea_p} + \frac{(1-\nu^2)}{\pi E a_p}\sum_{j=0}^{m} p_j \sum_{k=1, r_{ijk}\neq 0}^{n_j} \arcsin\left(\frac{a_p}{r_{ijk}}\right) \tag{3.10}$$

where E is the elastic modulus, ν is the Poisson's ratio, a_p is the effective radius of the square pillars and r_{ijk} is the radial distance of the given pillar on the i^{th} ring from the k^{th} pillar on the j^{th} ring. The first term gives the component of the displacement under the given pillar due to the self load (here $r_{ijk} = 0$).

From equations 3.8 and 3.10, we have:

$$\begin{aligned} \frac{(1-\nu^2)p_i}{2Ea_p} + \frac{(1-\nu^2)}{\pi E a_p}\sum_{j=0}^{m} p_j \sum_{k=1, r_{ijk}\neq 0}^{n_j} \arcsin\left(\frac{a_p}{r_{ijk}}\right) &= u_0 - \frac{h_i}{2} \qquad \text{i = 0,1,2,..,m} \\ &= u_0 - \frac{{r_i}^2}{4R_c} \end{aligned} \tag{3.11}$$

Thus, we have m+2 unknowns ($p_0, p_1, p_2, ..., p_m$ and u_0) and m+1 equations. For the final constraint, we require that, the sum of the loads on all pillars in contact should equal the total load applied on the lens for equilibrium:

$$P = \sum_{i=0}^{m} n_i p_i \tag{3.12}$$

From these equations, we can solve for the load distribution within the contact. To validate the approach, we modeled the stress distribution with 2μm size pillars on the flat and reduced the channel width from $10^{-1}\mu$m to $10^{-3}\mu$m. We assumed quartz to be isotropic and took E = 95600 MPa and ν=0.08 for all the simulations. As the channel dimension was decreased, the solution approached the Hertzian solution for a sphere pressed against a flat (Figure: 3-5(a)). We assumed a total load of 0.847 N on the lens and solved for the stress distribution and contact radius. For experiment PS52009 (8μm island channel structure), the mean stress on the central pillar was calculated to be 531 MPa while the outer most pillars saw a mean stress of 34 MPa (see Figure: 3-5(b)). We predicted 7 pillars across the diameter of the contact, which

is roughly consistent with the observations (Figure 4-9). Similarly, for experiment PS062309 (4μm island channel structure), the calculated mean stress on central pillar and outermost pillars were 554.6 MPa and 2.84 MPa, respectively (Figure 4-12(a)). We predicted 14 pillars across the diameter within the initial contact area for this experiment, which matches very closely within a region of SEM images revealing damaged pillars (Figure 4-12(a)). The mean stress on the pillars is compared with the classical Hertzian contact solution (Figure 3-5(b)). Note that the contact radius remains almost same, but the stress on the pillars is greatly amplified. The increase in stress on the pillars is proportional to the area occupied by the channels.

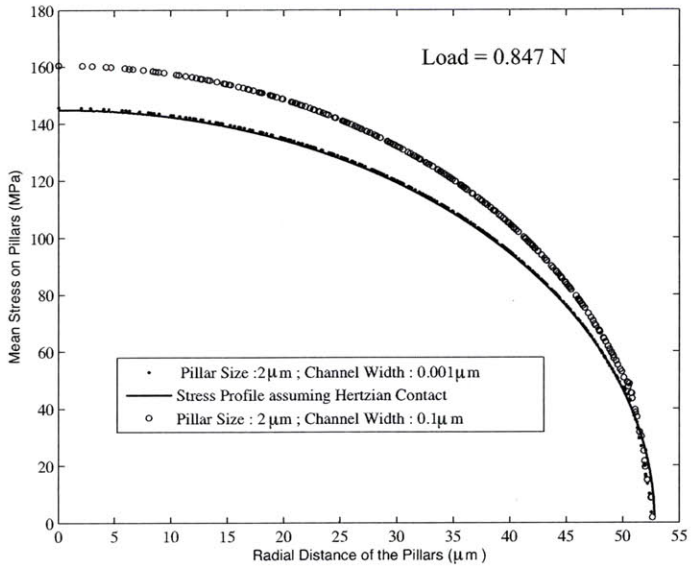

(a) Simulated stress profiles within contact while the channel width is decreased relative to the pillar dimension. Hertzian solution is approached as channel width is decreased.

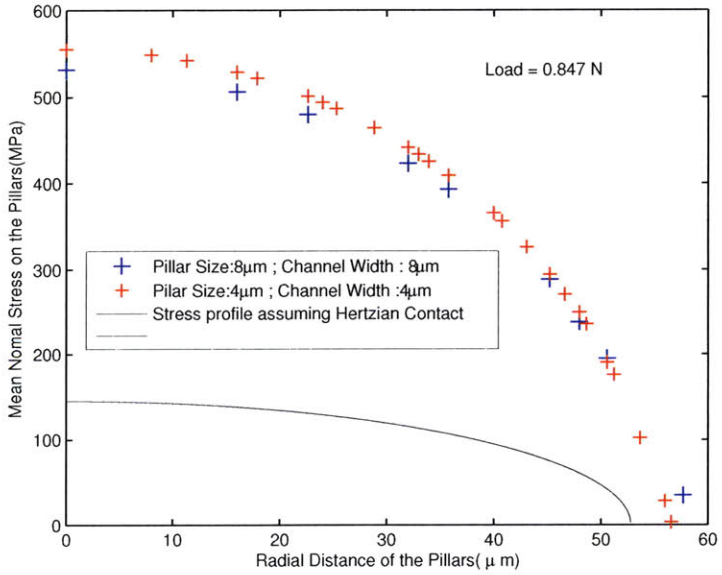

(b) Calculations of initial contact stresses appropriate to our experiments in comparison to Hertzian solution.

Figure 3-5: Simulated stress profiles

3.5 Refractive Index

Knowledge of the refractive index of the quartz solution was necessary to compute the lens separation from the order of the interference minima. We were not aware of any experimental data on refractive index of the silica-water solution at the experimental conditions and so assumed that the refractive index of the solution was same as that of water at 425^0C and 150 MPa. The mole fraction of dissolved quartz in water under these conditions is very small (7×10^{-4}) (Kennedy, 1950) and so the assumption is probably valid. The refractive index of water calculated using a software (Verma, 2003) based on the 'IAPWS 1995 formulation' (Wagner & Pruβ, 2002) was 1.2400, 1.2361, 1.2354 for wavelengths 431nm, 542nm, 575nm, respectively. Further, we estimated the refractive index of the solution from the slope of the line when the square of the radius of the interference fringes was plotted against the order number (Figures 4-1, 4-2). Equation 3.4 relates the slope to the refractive index. The value, thus calculated, was between 1.21 to 1.25.

3.6 Order Number of Interference Minima

In experiments PS062309 and PS052009, the contact was on the top of pillars and the interference pattern was formed from the reflections off the bottom of the channels. The central interference fringe, does not necessarily mark the edge of the contact region. The order of the central fringe depends upon the height of the pillars at the center and the refractive index of the medium. In our experiments, although the initial fabricated structure was well characterised, it might be possible that during setting up the experiment or due to rolling of the lens, the pillars might be crushed. Use of variable wavelength light source is one way in which the extant of pillar crushing at the start of an experiment can be diagnosed. Hickman (1992) found the order of the interference fringes and the seperation between the lenses by monitoring the change in wavelength required to offset the interference minimum at a given location by one order. In the present set of experiments, the interference fringes moved very

little with the change in wavelength possible with our apparatus, because the radius of curvature of the lens in our experiments was smaller than that used in Hickman's experiments (about 1 cm vs about 10cm). This limits the use of that method to our problem.

Instead, we tried to estimate the initial lens separation/pillar height by matching the radii of interference minima observed at the start of the experiments with those theoretically calculated by varying the initial lens separation. The interference patterns should match when the initial lens separation is assumed right. From equation 3.4 and assuming elastic convergence (s = δ_e, mutual elastic approach), the radius of interference minima is given by:

$$r_m = \sqrt{2R_c\left(\frac{m\lambda}{2\mu} + \delta_e - h_0\right)} \tag{3.13}$$

The elastic approach of the two lenses assuming Hertzian contact (Johnson, 1985) is :

$$\delta_e = \sqrt[3]{\frac{9P^2}{16R_cE*^2}} \qquad \text{where } E^* = \frac{E}{1-\nu^2} \tag{3.14}$$

where P is the applied load. We calculated the elastic convergence to be 0.2479 μm for a load of 0.847 N. The simulations for contact stress profile, discussed in the previous section, suggest that the elastic approach should be 0.2620μm, 0.2548μm when the quartz flat has 8μm, 4μm size island channel structures, respectively (for a load of 0.847 N). The initial plastic deformation is probably an order of magnitude less than the elastic deformation and does not affect these calculations much. We applied this to experiments PS052009 and PS061309 and matched with the radius of interference minima from the observed interference patterns. For a given wavelength, the observed and calculated pattern matches at discrete pillar heights separated by $\frac{\lambda}{2\mu}$. So, we looked at three different wavelengths (542 nm, 575 nm, 431nm) and picked the common pillar height. This estimated pillar height was 1.02±0.02 for PS052009 and 0.52±0.02 for PS062309, values which match the fabricated pillar heights (Table B.1). The interference minima order numbers were calculated, knowing the separation between the lenses.

Chapter 4

Results

A total of 4 experiments with different surface morphologies (Table 4.1) were conducted in this study. We started with no surface morphology on the quartz flat in experiment PS031209 and introduced etch pits in experiment PS041309, and island-channel structures with varying pillar and channel sizes in experiments PS052009 and PS062309 (Tables 4.1, B.1). The quartz lenses (both plano-plano and plano-convex lenses) used in the experiments were Y-cut single crystals, with lens bases cut parallel to the $(1\bar{1}00)$ plane. The plano-convex lenses had a radius of curvature of 0.443 inch. We tried to maintain a grain boundary twist angle of $20\text{-}30^0$ in the experiments. All the experiments were conducted in a saturated quartz solution at 150 ± 1 MPa fluid pressure, while the measured temperature close to the contact varied from 414^0 to 418^0C for the four experiments (see Table 4.1). The applied load varied from 0.8466 N to 0.8476 N. The variation in the load was due to the change in the mass of quartz weights used in the experiments. The quartz weights were weighed before and after each experiment and they showed a slight decrease in weight after each experiment due to the dissolution of quartz in the initially distilled water as it came up to saturation. The pressure vessel was sealed at a pressure close to 50 MPa and the temperature was slowly raised from the room temperature in three steps, 300^0C, 350^0C, 425^0C, each taking about 1.5 hours. Pressure was always maintained above 50 MPa ensuring that water does not undergo phase transition to steam before it enters the super-critical regime.

Experiment	PS031209	PS041309	PS052009	PS062309
Quartz Flat	Sample 1	Sample 5	Sample 2	Sample c1
Surface morphology	smooth	$\triangle^{lr}$ etch pits	8μm pillars	4μm pillars
Load(N)	0.8465±1	0.8476±2	0.8471±1	0.8467±1
Temerature, T (^{0}C)	417±1	417±1	414±1	418±1
Fluid Pressure, p_f (MPa)	150±1	150±1	150±1	150±1
Mean Normal Stress, p_m(MPa) (at the start of exp.)	81±2	94.5±5	443±65	417±118
Time, t(hrs)	450±4	433±4	477±4	472±4
Convergence, s (μm)	no	no	no	0.15±0.02

Table 4.1: Summary of the experiments

For all but one experiment, PS031209, a manual pressure generator was backed off as the temperature was raised to prevent the over-pressuring the vessel due to thermal expansion of water. In this experiment, however, while rising the temperature, the valve connecting the pressure vessel to the pressure transducer was accidentally closed, preventing us from being able to read the increase in the fluid pressure with temperature. When we rectified this problem, the fluid pressure in the system (pressure vessel, piping and the pump) read 120 MPa. During this process, two cracks initiated near the contact between the two lenses (Figure 4-3). Assuming the same compressibility for the vessel and the rest of the system, the pressure in the vessel when accidentally isolated was estimated to be 178.6 MPa. The temperature and fluid pressure in the vessel were then brought to 342^{0}C and 80 MPa respectively, and held stable for 20 hours to allow the cracks to heal and stabilize. Then the temperature and pressure were raised to the run conditions of 417^0 C and 150 MPa over an hour and the experiment was carried out for 450 hrs.

4.1 Contact Morphologies

The crack that formed under the contact in experiment PS031209 was stable throughout the experiment, and the contact did not evolve during the experiment (Figure 4-3). The recovered contact on the quartz flat is shown in the Figure 4-7. Similarly, Figures 4-4(a) and 4-4(b) show the contact in experiment PS041309 at the start and end of

the experiment. The contact had a channel, composed of etch pits, running through the center (see Figures 4-4(b) and 4-8). In neither experiment did the recovered contact show any morphological evidence of pressure solution or neck growth.

The contact size was the same at the start and end of the experiment PS052009 (Figures 4-5(a), 4-5(b)). But, the recovered contact on the quartz flat (see Figure 4-9) showed significant evolution in the surface morphology throughout the surface of the flat. The pillars, which were initially square in shape (see figure 2-1(a)), grew by about 7μm along the c-axis $< 0001 >$ of the crystal, closing the channels perpendicular to the caxis (see Figures 4-10, 4-11). The growth direction was same through out the surface of the flat. Iwasaki (1997) measured the growth rate anisotropy of synthetic quartz grown in Na_2CO_3 solution and found that the ratio between the growth rate of the basal plane (along c-axis, see Figure 4-16) and the prismatic m face (the top of the pillars, edges parallel to c-axis) is around 60. The ratio between the growth rate of the rhomb r face (the inclined planes in the grown pillars) and the prismatic m face is close to 10. Our observations are consistent with the rates reported by Iwasaki.

The pillars outside the contact evolved different from those inside the contact. Pillars outside the contact faceted on the top and grew uniformly in the direction of c-axis (see figure 4-10). Pillars inside the contact grew forming 'c' shaped structures, probably, due to faster growth at the corners (see Figure 4-11(a)). The corners might have acted as nucleation sites due to the stress concentration and grew faster consuming silica from the pore fluid in the channel. At the same time, the interior of the face might not have free access to the pore fluids in the channel, hindering its growth. Inside the contact, the top surfaces of the pillars, which would have been in contact with the lens surface, had small indentations that are reminiscent of intergranular fluid inclusions (Figure 4-11(b)). We could not recover the contact region with the upper lens in place and thus can only conjecture that this region had formed into a grain boundary during the experiment. We could see faceting inside the pits, which also suggests that the structure was not moving rapidly. Outside that region, the surface of the pillar looked relatively smooth or faceted in some cases (Figure

4-11(b)). Thus, we conclude that the newly grown regions of the pillars inside the contact were not in contact with the lens.

The sample recovered from experiment PS062309 showed similar growth of pillars along c-axis as discussed above. But the growth of the pillars was limited only to those pillars which were considerable away from the contact. Figure 4-15 shows the pillars that grew away from the contact. Within the contact, the SEM photomicrographs reveal crushing of pillars and fracturing (Figure 4-12). Some pillars completely disappeared 4-12, while some showed undercutting 4-13.

4.2 Contact Stresses

The mean normal stress p_m in each of the experiments was calculated by knowing the load and measuring the contact area. In experiments PS031209 and PS041309, we could see the central dark spot/spots in the interferograms (Figures 4-3, 4-4). These central dark spots correspond to the zeroth order minima and are the actual contact between the two lenses. We measured the area by counting the pixels on the interferogram and scaling them. The mean normal stress in experiments PS031209 and PS041309, accounting for uncertainty in the load and the uncertainty in the contact area measurements, was 81 ± 2 MPa and 94.5 ± 5 MPa respectively.

But in experiments PS052009 and PS062309, when the interference pattern was formed at the bottom of the channels, it was not straightforward to calculate the contact area from the interferograms. Here, the central interference fringe does not mark the edge of the contact region. The contact region can have more than one interference maxima or minima if the pillars are deformed. So, we looked at the recovered contact on the quartz flats to estimate the contact area. The SEM photomicrographs of the contact on the recovered quartz flats from experiments PS052009 and PS062309 showed features distinguishing the pillars inside and outside of the contact.

Figures 4-10 and 4-11 show the top of the pillars inside and outside the contact in the experiment PS052009. Based on the indentation marks on top of pillars, which suggest formation of inter-granular boundary, we identified the pillars within the

contact. Figure 4-9 shows the contact region on 'Sample 2'. Though the sides of the pillars grew, the actual surfaces of the slid-solid appeared to remain constant. Figure 4-11 shows a single pillar inside contact. Note that the grown portion of the pillar is smooth, implying no contact. Knowing the initial size of the pillars and counting the number of pillars inside contact we measured the contact area in experiment PS052009. Interestingly, the number of pillars in contact (34 ± 1) match with the number of pillars expected to be in contact from the simulations (37). The central fringe radius in the interferogram also matches the observed contact radius. The dimensions of the portion of pillar in contact, as observed from SEM photomicrographs, varied from $7.1\mu m \times 7.1\mu m$ and $7.9\mu m \times 7.9\mu m$. Accounting for this variation, we calculated the initial mean normal stress to be 443 ± 65 MPa. The simulation results shown in Figure 3-5(b) were conservative and assumed pillars to be $8\mu m \times 8\mu m$ and thus the stress levels in the simulations are less than the mean normal stress quoted from the experiments.

Estimating the mean normal stress in experiment PS062309 was more challenging. We identified the contact spot on the recovered quartz flat (Sample c1) by matching with scratches and other features observed on the interferogram taken during the experiment. Unlike the previous case, we did not see any difference in the surface morphology on the top of the pillars inside and outside the contact. Except that some pillars inside the contact, closer to the center of the contact, were crushed or deformed (Figure 4-12(a)). From the interference pattern observed under 431 nm wavelength illumination, the radius of the minima corresponding to a separation of $0.52\mu m$ was $58\mu m$ and $89.6\mu m$, at the start and end of the experiment, respectively. This should approximately correspond to the range of the contact radius, since the fabricated pillar height was $0.55\mu m$. Even, the numerical simulations estimate the initial contact radius to be $56.5\mu m$. Assuming an initial contact radius, the contact radius at every observation time was calculated by knowing the convergence until that time (from equation 3.5) . For the calculations, the initial contact radius was allowed to vary, about the radius of interference fringe corresponding to $0.52\mu m$ lens separation, from $55\mu m$ to $65\mu m$. The estimated values of final contact radius

were 76μm to 83μm, correspondingly. Moreover, some pillars were crushed inside the initial contact area. Crushing might have occured during the loading of the lens or during the experiment. So, there is uncertainty in the mean stress estimated though we knew the exact contact radius. To estimate contact stress, we considered two extreme cases: either none of the pillars were crushed at the start of the experiment, or up to 1/3 of the pillars in the initial contact area failed. Allowing for uncertainty in the number of intact pillars and the uncertainty in the initial contact radius, we estimated the initial and final mean normal stresses to be 417±118 MPa and 178±23 MPa, respectively.

4.3 Convergence

Convergence was calculated from equation 3.4 following the method described in section 3.1. As we mentioned before, it is the time-dependent component of convergence ($\Delta s = s(t)-s(0)$) that we are referring to as convergence here. The square of the radius of interference minima plotted against order number is shown for the experiments PS031209 and PS052009 in the Figure 4-1. Within the experimental error, the radius of the interference minima did not change during the course of the experiments, indicating no convergence. In experiment PS041309, the interference pattern was complicated (Figures 4-8) and thus we could not measure the radii of interference fringes. For this experiment, convergence is qualitatively measured by overlaying the interference patterns on one another in transparent overlays. There was no change in the interference patterns taken at 19hrs after the start of the experiment and those taken at the end of the experiment. The photomicrographs from the start of the experiment to 19hrs were too distorted to interpret. Thus, there was no observable convergence in the experiments PS031209, PS041309 and PS052009.

Convergence was observed only in one case, i.e., experiment PS062309. The total convergence in 472 hours was 0.15±0.02μm. Convergence was rapid initially and slowed with time (see Figure 4-2). The average convergence rate over the experimental duration was 0.007μm/day. When the convergence data was fit to a power-law of the

form Δ s = $\alpha' t^{\beta'}$, we obtained $\alpha' = 0.02228$ and $\beta' = 0.3134$ with a R square goodness of fit of 0.9607; Using the above fit we calculated the instantaneous convergence rates at t = 4 hrs , t=470 hrs to be $2.7\times10^{-3}\mu$m/hr and $1.02\times10^{-4}\mu$m/hr.

It should be noted that the convergence observed in PS062309 is associated with recovered micro-structures indicative of fracturing, suggesting that cataclysis may have played an important role in convergence (discussed in discussion).

4.4 Figures

Figure Captions

Figure 4-1 The square of the radius of interference minima (looked under 431nm, 542 nm, 575 nm) is plotted against the order number at the start(Δ) and end($\times$) of the experiments PS031209 and PS052009. The data indicates no convergence. The lines should shift to the right preserving the slope when the lenses converge. The constant slope of the line indicates a constant radius of curvature.

Figure 4-2 (a) The square of the radius of interference minima is plotted against the order number at different elapsed times for the experiment PS062309 (wavelength 431 nm). The lines shift to the right preserving the slope, indicating convergence.(b) The convergence of lenses after initial loading ($\Delta s = s(t) - s(0)$) is plotted against elapsed time. Convergence is rapid initially and slows down as time proceeds.

Figure 4-3 Comparison of interferograms at the start (Figure 4-3(a)) and the end (Figure 4-3(b)) of experiment PS031209. The fringes did not move out. But, note that the contact moved a little bit. The branch of the trilobite shaped crack, above the contact, was not completely under the contact at the start of the experiment. Analysing the crack under optical microscope revealed that it actually lies below the surface. Also, note the fine crack which passes through the center of the contact. This caused the first few fringes to be displaced.

Figure 4-4 Comparison of interferograms at the start (Figure 4-4(a)) and the end (Figure 4-4(b)) of experiment PS041309. Because of the triangular etch pits, there were no trackable circular fringes. The contact was at two spots as pointed out in the figure. Fringes can be observed in the channel (series of etch pits) that passed through the center of the contact. The area occupied by the two dark spots was measured and considered as the contact area. We were unable to take a good image until first 19 hours.The interferograms were over laid over one another to measure convergence

qualitatively. We observed no convergence.

Figure 4-5 Comparison of interferograms at the start (Figure 4-5(a)) and the end (Figure 4-5(b)) of experiment PS052009. The fringes were stationary through out the experiment.

Figure 4-6 Comparison of interferograms at the start (Figure 4-6(a)) and the end (Figure 4-6(b)) of the experiment PS062309. The fringes moved out with time suggesting convergence.

Figure 4-7 SEM photomicrograph of the recovered contact spot on Sample 1 (Experiment PS031209). The contact region is marked.

Figure 4-8 SEM photomicrograph of the recovered contact spot on Sample 5 (Experiment PS041309). The channel marked in the interferogram (Figure 4-4(b)) can be observed in the photomicrograph. The maximum width of the channel within the contact was 120μm.

Figure 4-9 SEM photomicrograph of the recovered comntact spot on Sample 2 (Experiment PS052009). The contact is within the yellow circle. The surface structure on the top of pillars within and outside the contact is different (compare Figures 4-10 and 4-11). Based on this, we identified the number of pillars within the contact region and thus the contact area. Note that the pillars outside the contact grew until they touch, while the pillars inside tend to form fluid inclusion like structures.

Figure 4-10 (a) SEM photomicrograph of the pillars outside the contact in experiment PS052009. The pillars, which were initially square, have grown in one direction (along crystallographic c-axis) closing the channel. There was no significant change in the pillar dimensions in other directions. (b) SEM photomicrograph of the top of a pillar outside the contact. Faceting can be observed on top of the pillars.

Figure 4-11 (a) SEM photomicrograph of the pillars inside the contact region in experiment PS052009. The pillars, which were initially square, have grown in one direction (along crystallographic c-axis). Unlike the pillars outside the contact, they donot close completely along the c-axis. The evolution is governed by surface tension and they tend to form fluid inclusion like structures. (b) SEM photomicrograph of the top of a pillar inside the contact. We don't see any faceting because the surface was not exposed to free pore fluid. Also, observe the structures on the top which resemble fluid inclusions. The sharp edges within the structures imply that the structures were there for a long time and were not dynamic. Since we could not recover the same spot on the lens, we cannot say conclusively whether they were fluid inclusions. The spherical particles found in the images are due to metal coating for SEM imaging and should not be interpreted.

Figure 4-12 (a) SEM photomicrograph of the recovered contact spot on sample c1 (Experiment PS062309). The initial contact region is approximately within the marked circle. We arrived at this by looking at the deformed pillars and locating the center of the contact by matching the existing cracks and damage zones on the interferogram and the photomicrograph. (b) A higher resolution image of the the contact area. We could see hertzian contact cracks and crushed pillars. The regions marked with the green squares indicate an initially existing pillar at that location which was crushed and removed completely. The regions indicated with the yellow squares are magnified in Figures 4-13 and 4-14.

Figure 4-13 SEM photomicrographs of pillars inside the contact in experiment PS062309 (a) The pillar was deformed initially and then evolved with time. Undercutting can be observed at the center of the pillar due to the high stresses taken by it. (b) Pillars with cracks through them could facilitate high stresses and thus undercutting.

Figure 4-14 SEM photomicrographs of pillars inside the contact in experiment PS062309 (a) A pillar punched into the surface causing the cracks associated with a square punch (b) A pillar which is relatively undeformed.

Figure 4-15 SEM photomicrographs of pillars far outside the contact in experiment PS062309. The blue square box indicates the initial pillar location and dimension. Note that the pillars grew along the c-axis. But, the pillars did not close the channels completely in the direction of the growth.

Figure 4-16 Crystallographic planes on the grown pillars. The pillar shown in the figure was a pillar outside the contact on sample c1, in experiment PS062309. Same faces were exposed on the 8μm size pillars in experiment PS052009.

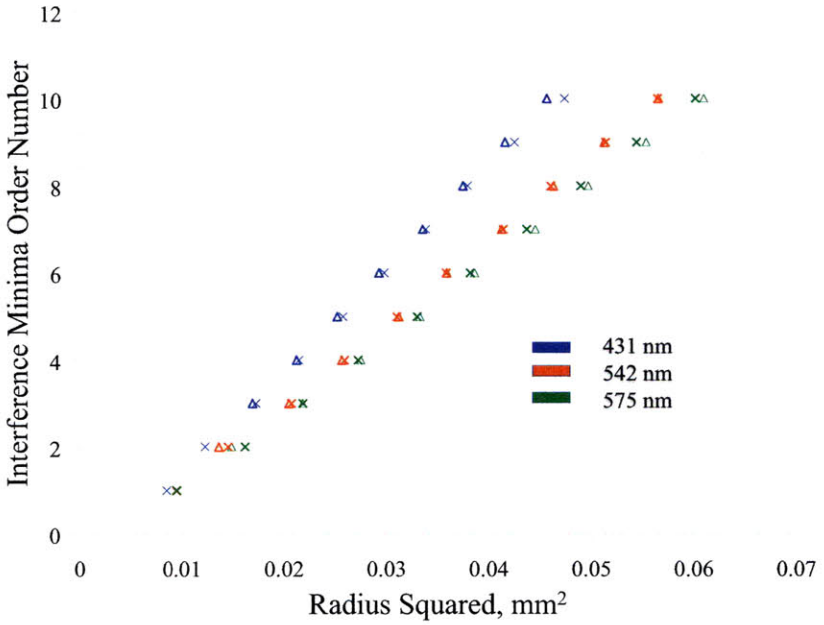

(a) Experiment PS031209

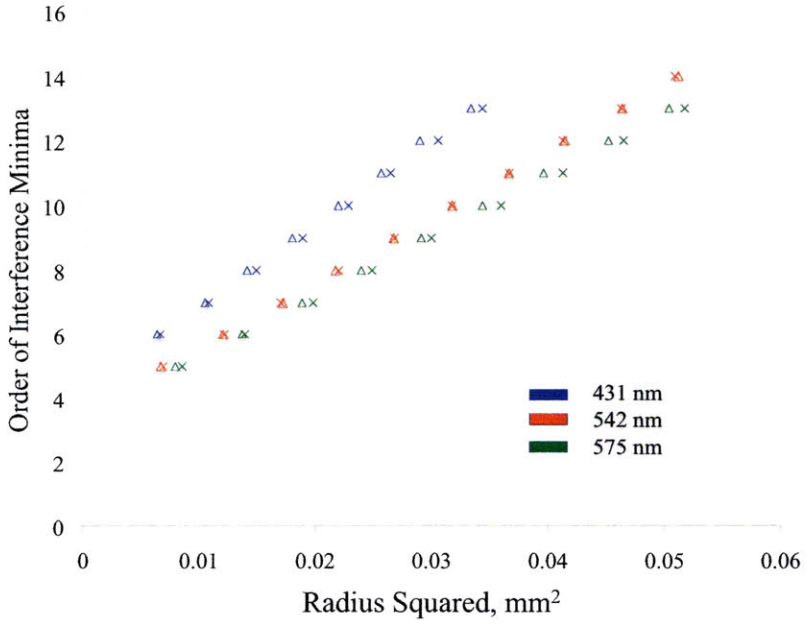

(b) Experiment PS052009

Figure 4-1:

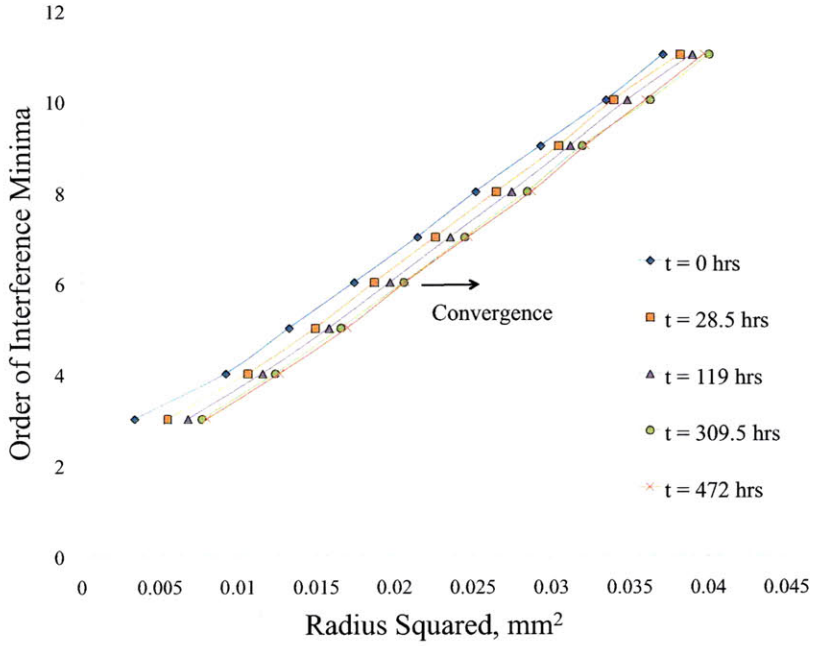
Order of Interference Minima
Radius Squared, mm2
Convergence
t = 0 hrs
t = 28.5 hrs
t = 119 hrs
t = 309.5 hrs
t = 472 hrs
0
2
4
6
8
10
12
0
0.005
0.01
0.015
0.02
0.025
0.03
0.035
0.04
0.045

(a)

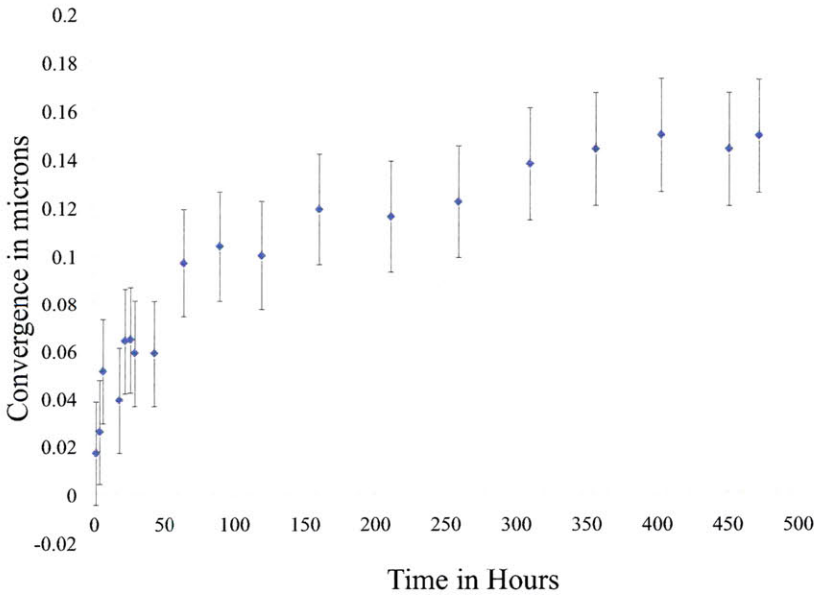
Convergence in microns
Time in Hours
-0.02
0
0.02
0.04
0.06
0.08
0.1
0.12
0.14
0.16
0.18
0.2
0
50
100
150
200
250
300
350
400
450
500

(b)

Figure 4-2:

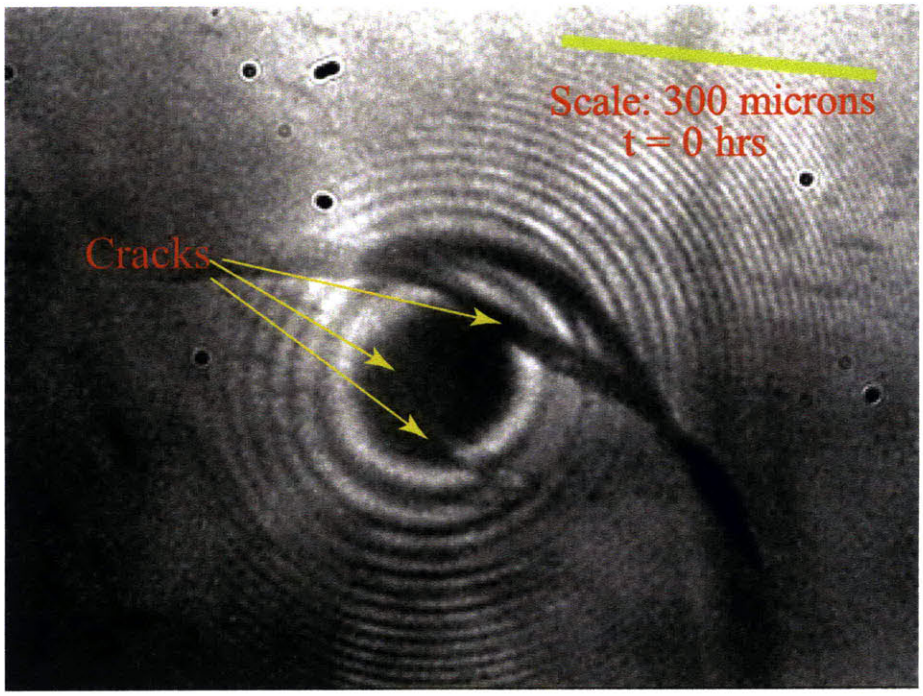

(a) Interferogram at the start of experiment PS031209

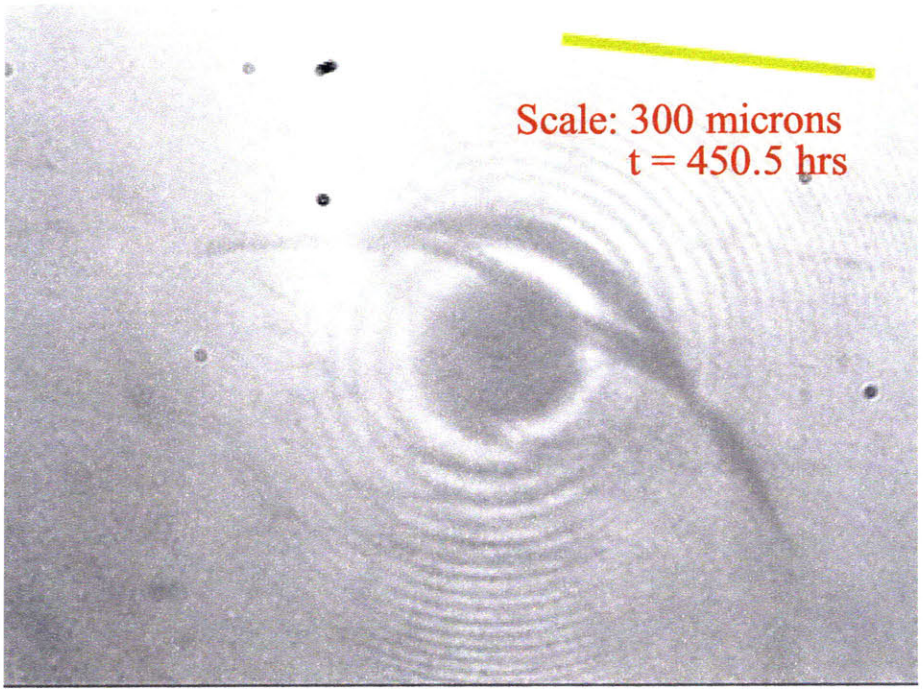

(b) Interferogram at the end of experiment PS031209

Figure 4-3:

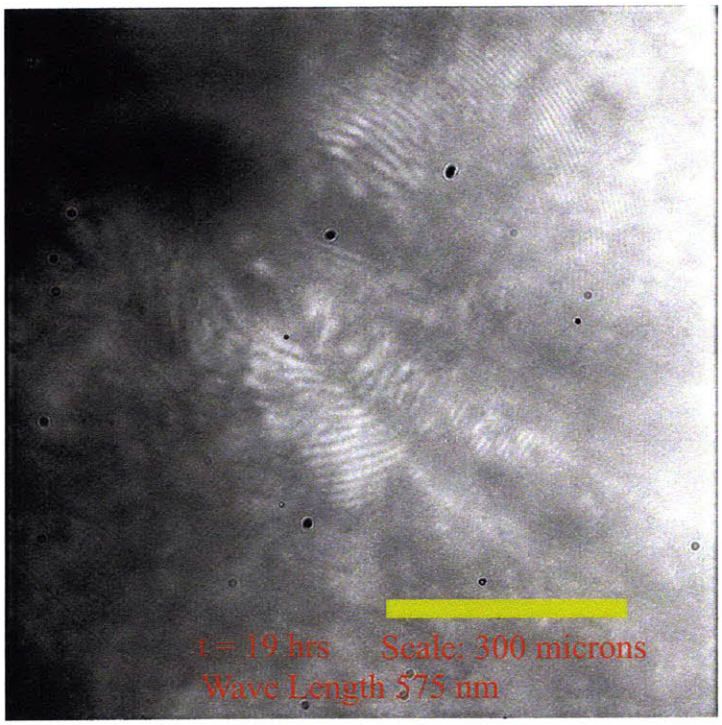

(a) Interferogram at the start of experiment PS041309

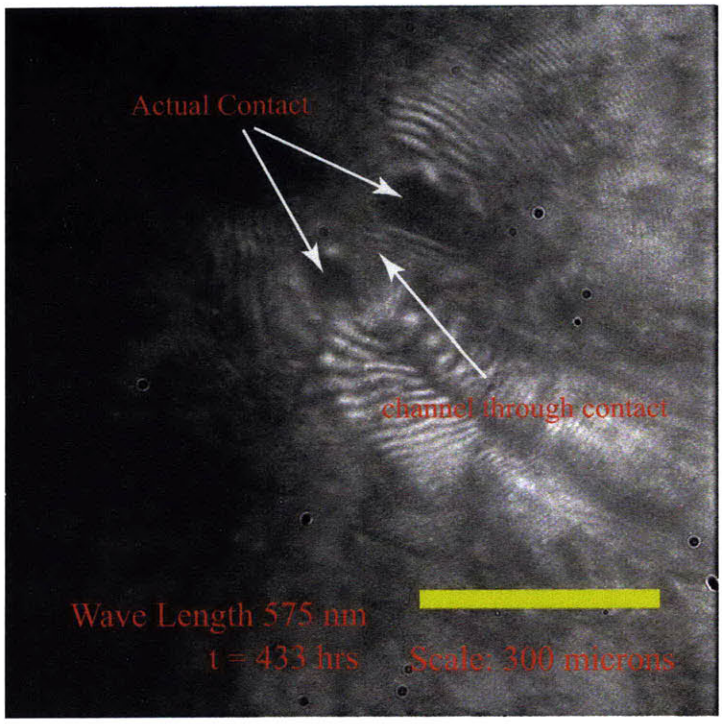

(b) Interferogram at the end of experiment PS041309

Figure 4-4:

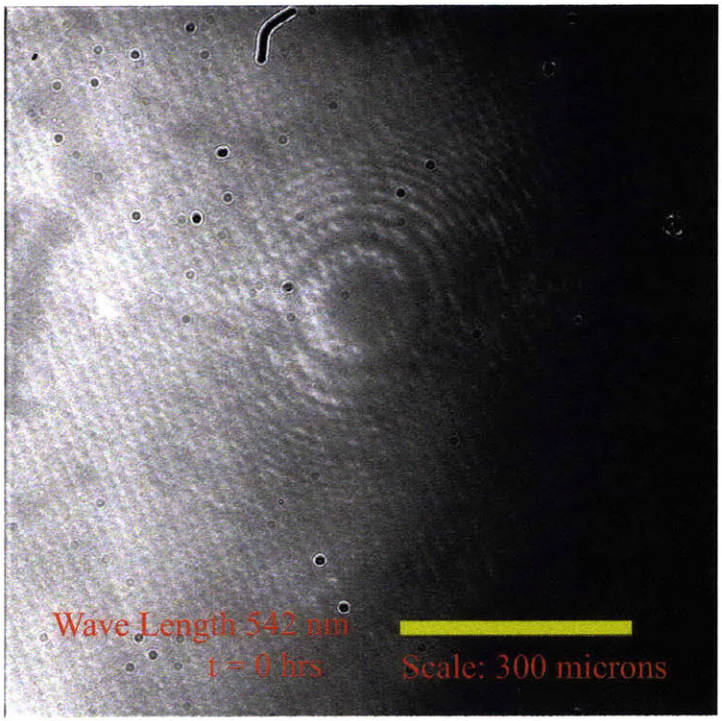

(a) Interferogram at the start of experiment PS052009

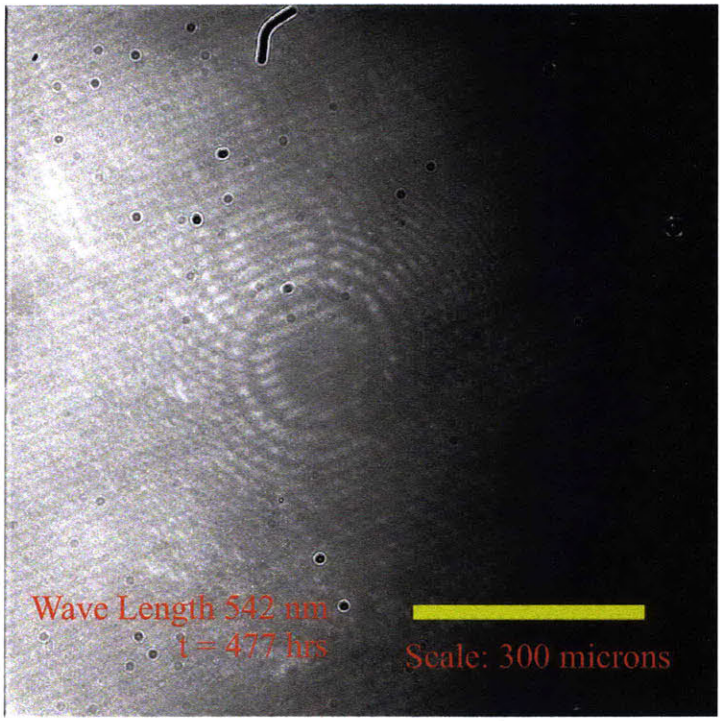

(b) Interferogram at the end of experiment PS052009

Figure 4-5:

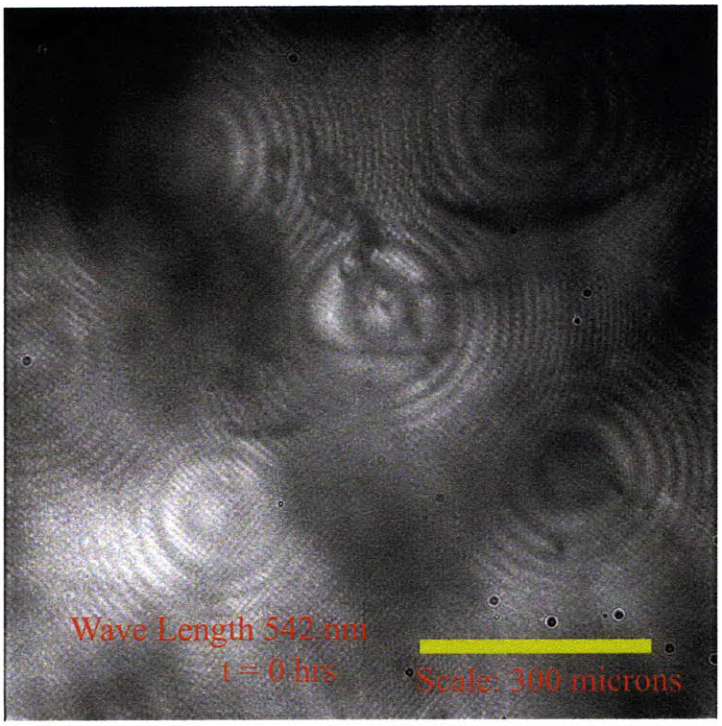

(a) Interferogram at the start of experiment PS062309

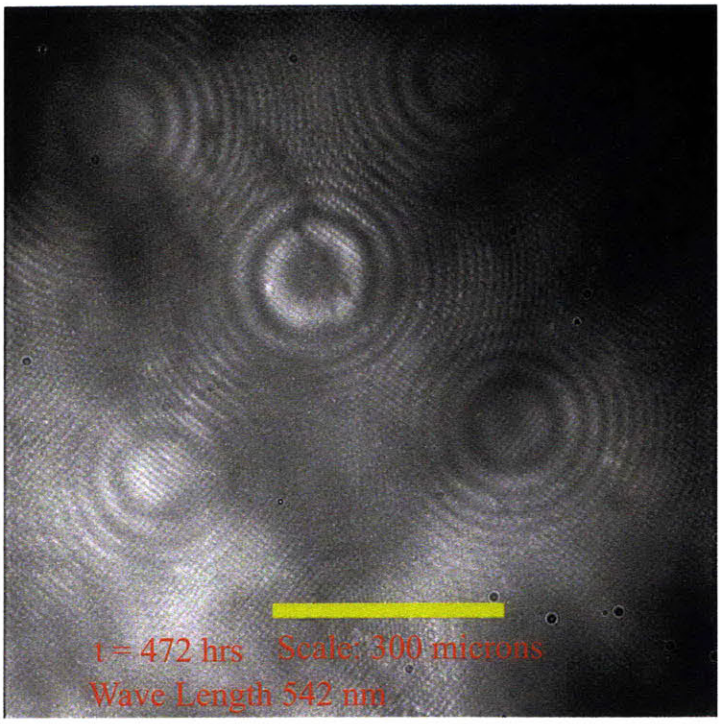

(b) Interferogram at the end of experiment PS062309

Figure 4-6:

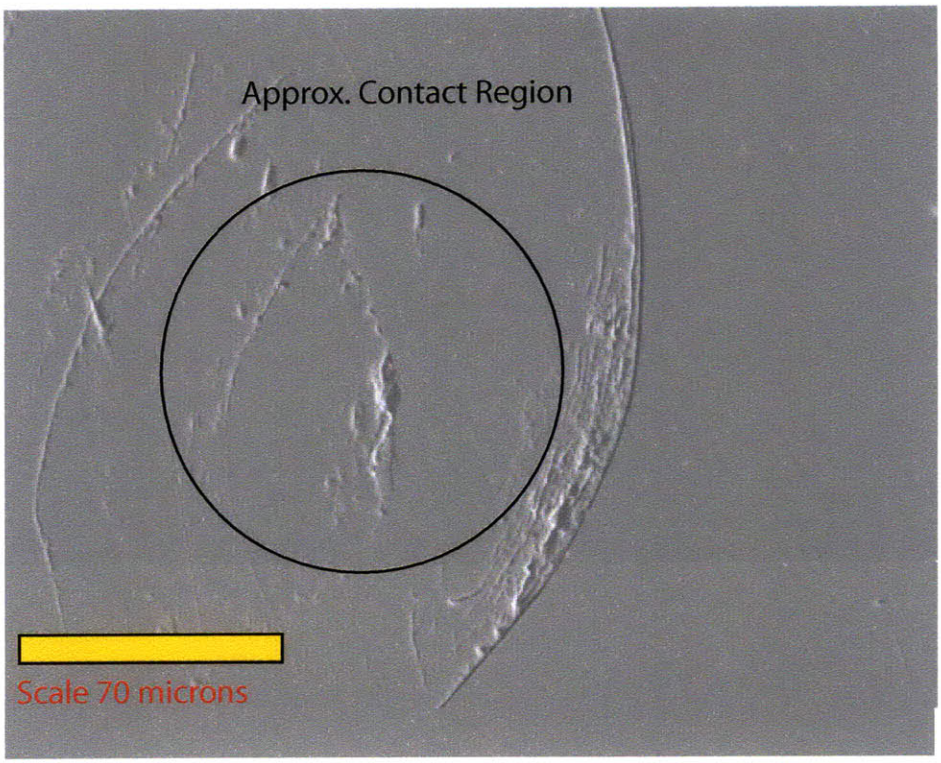

Figure 4-7:

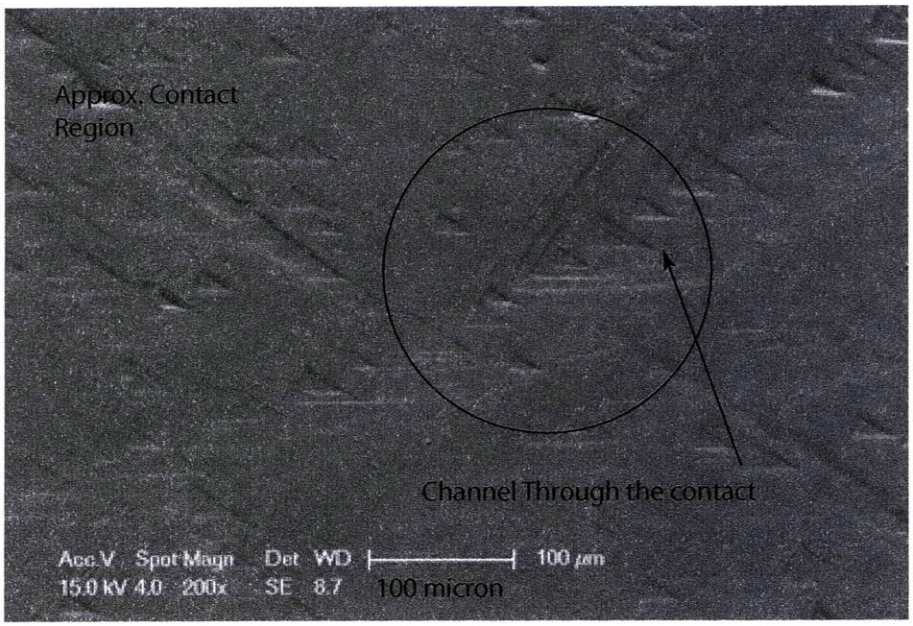

Figure 4-8:

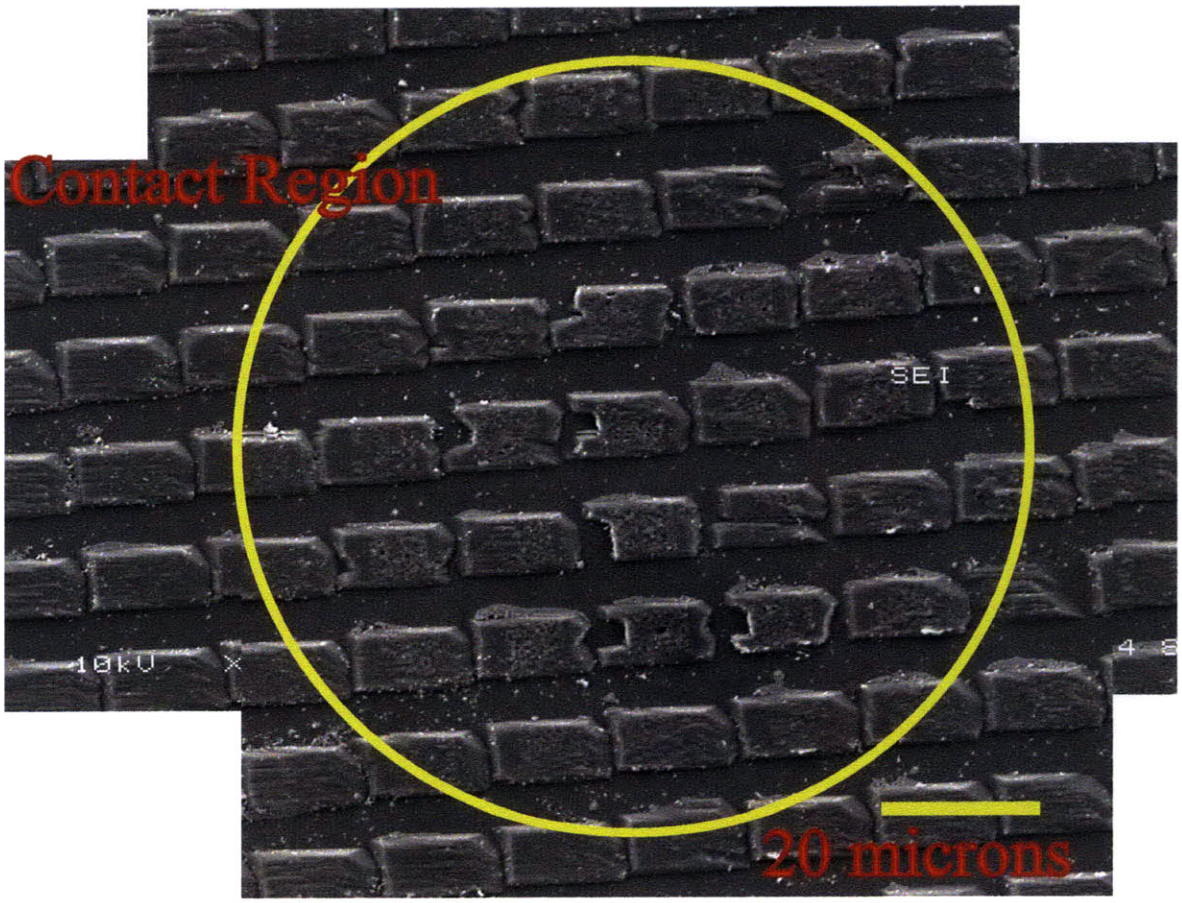

Figure 4-9:

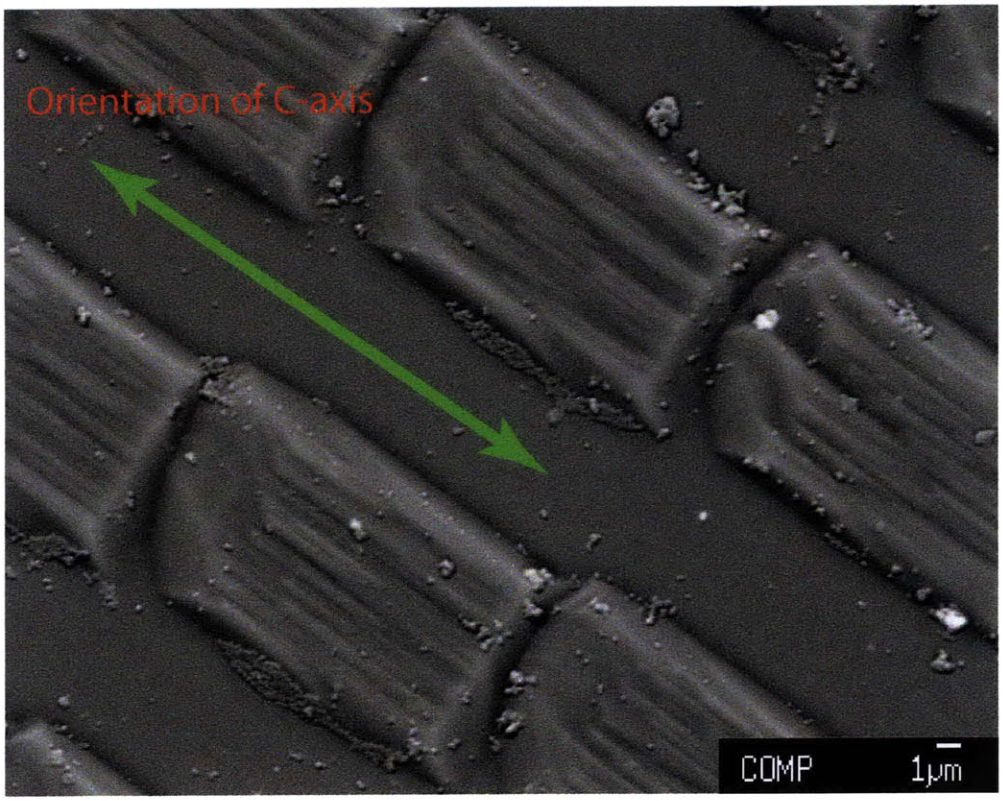

(a) Pillars outside the contact region in experiment PS052009

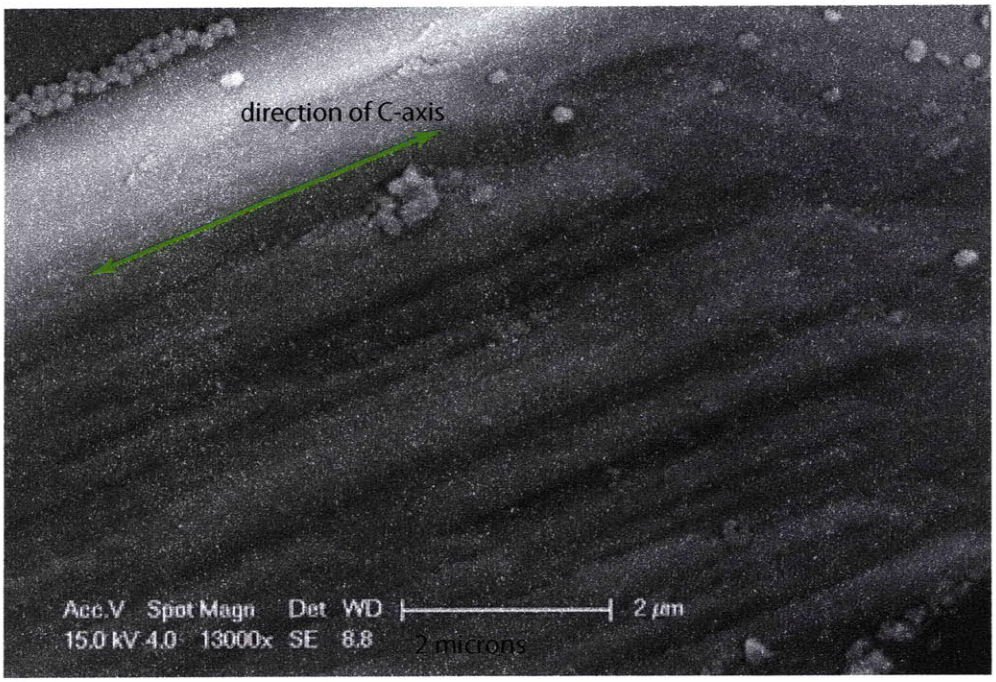

(b) Top of a pillar outside the contact region

Figure 4-10:

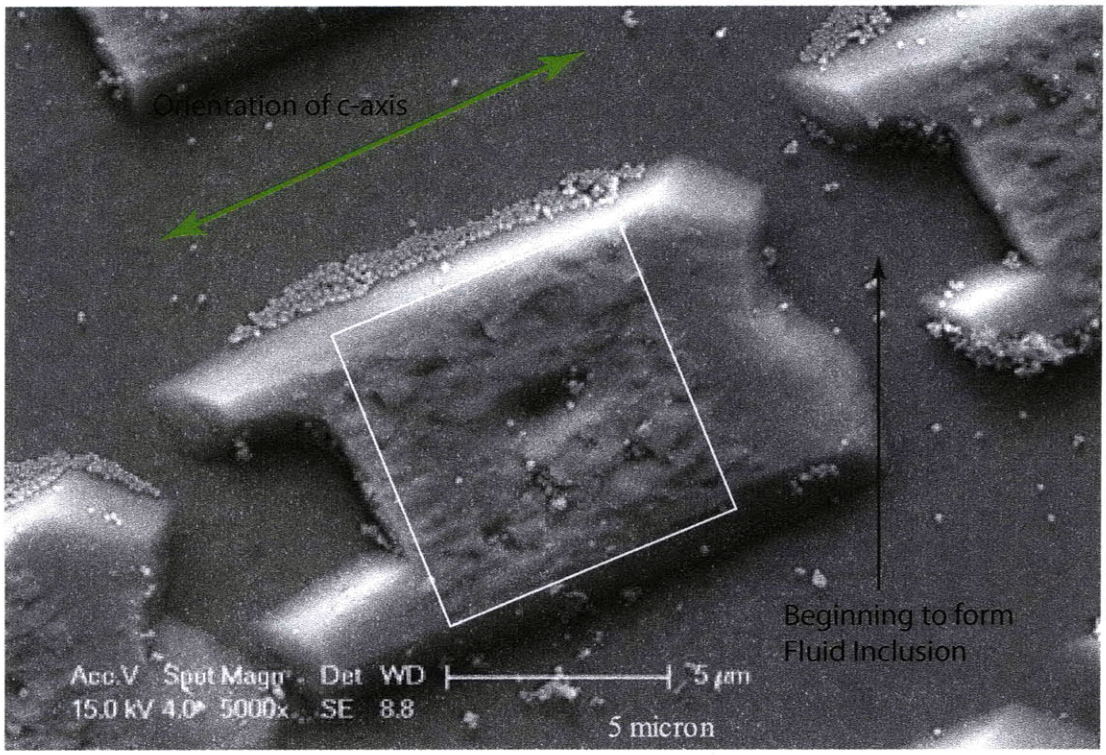

(a) Pillar inside the contact region in experiment PS052009

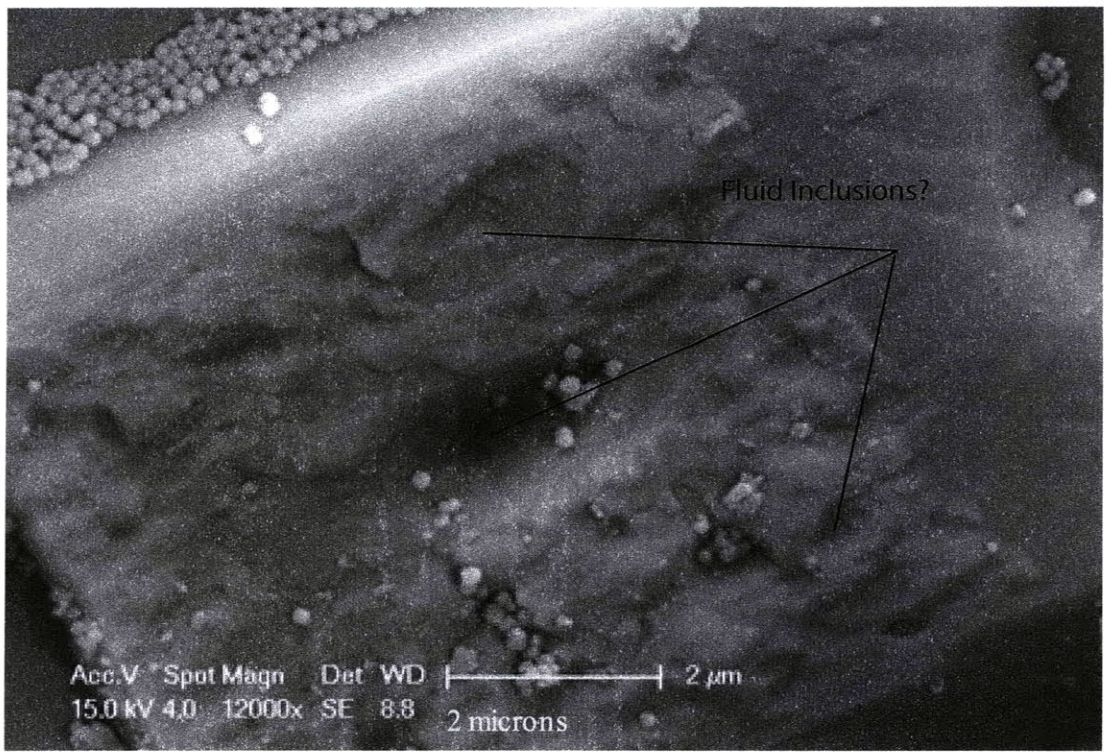

(b) Top of a pillar inside the contact region

Figure 4-11:

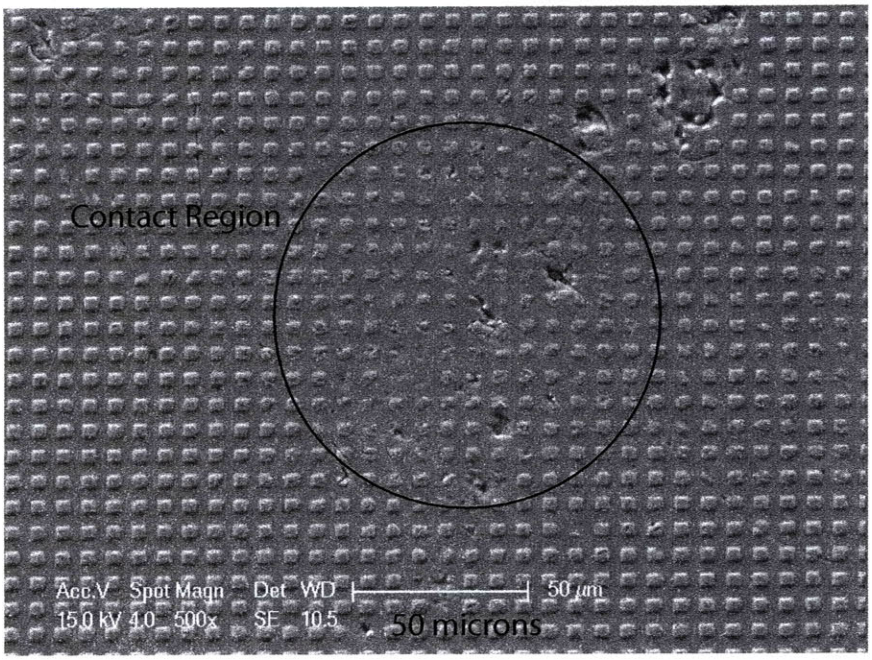

(a)

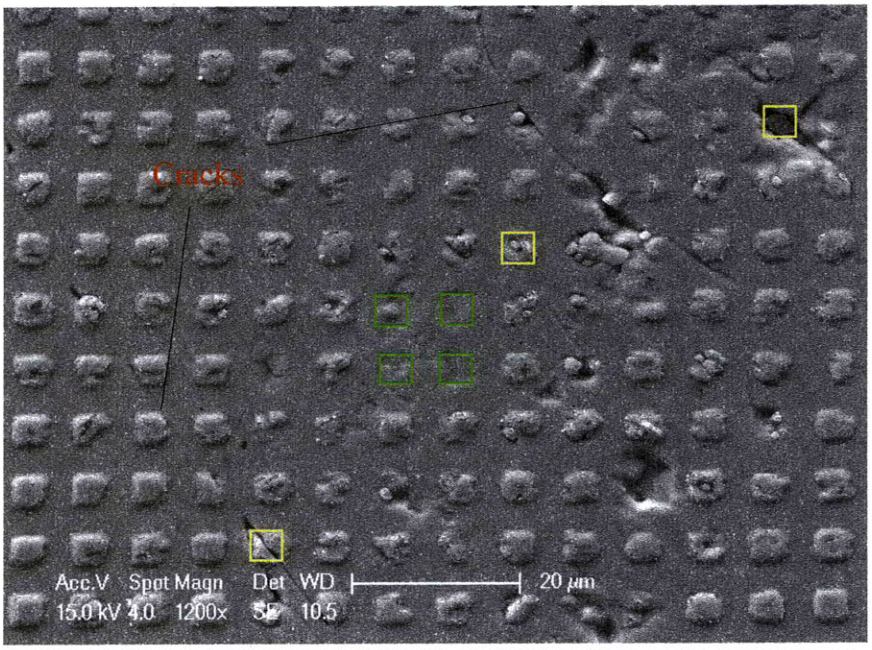

(b)

Figure 4-12:

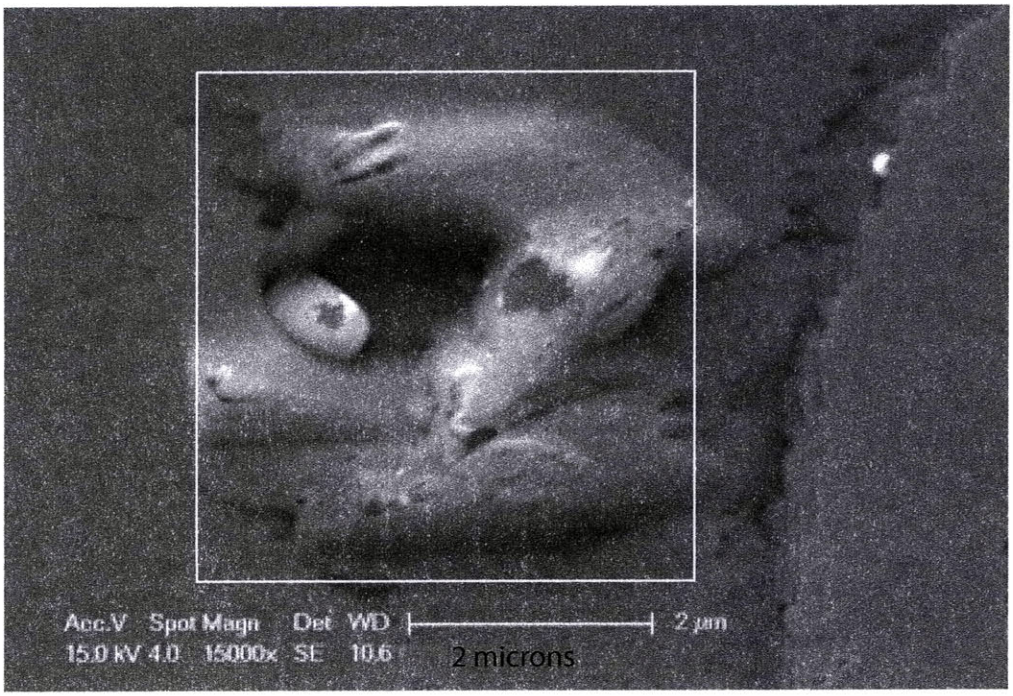

(a)

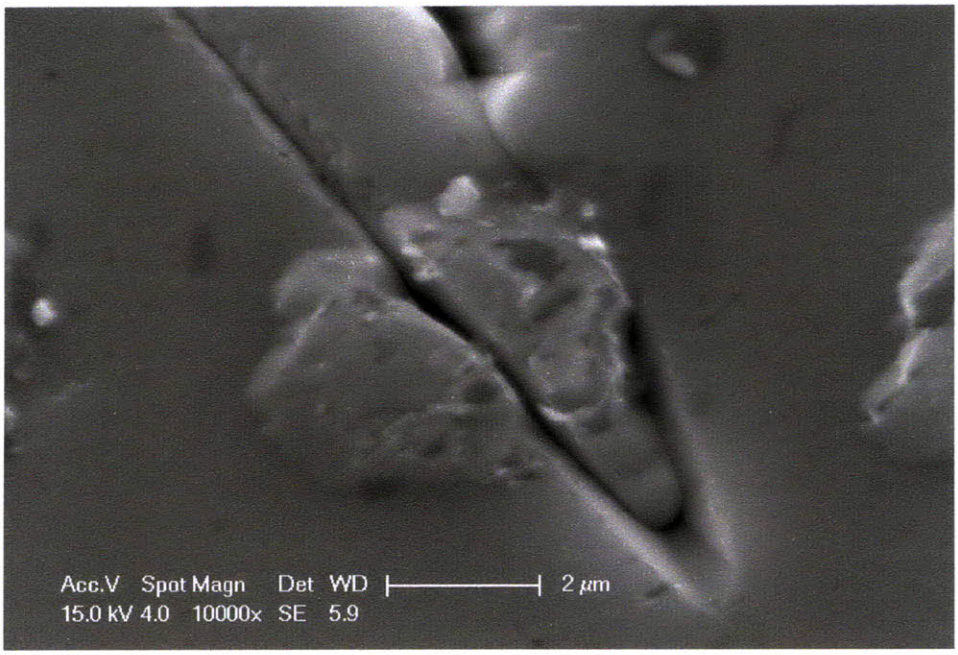

(b)

Figure 4-13:

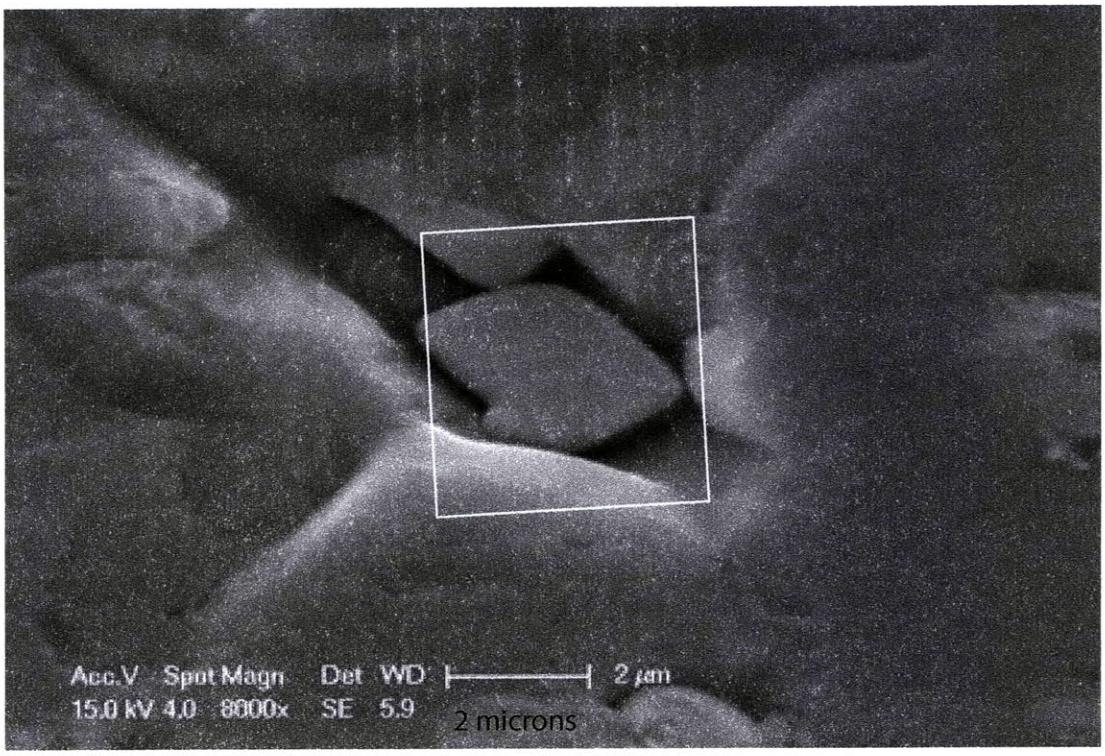

(a)

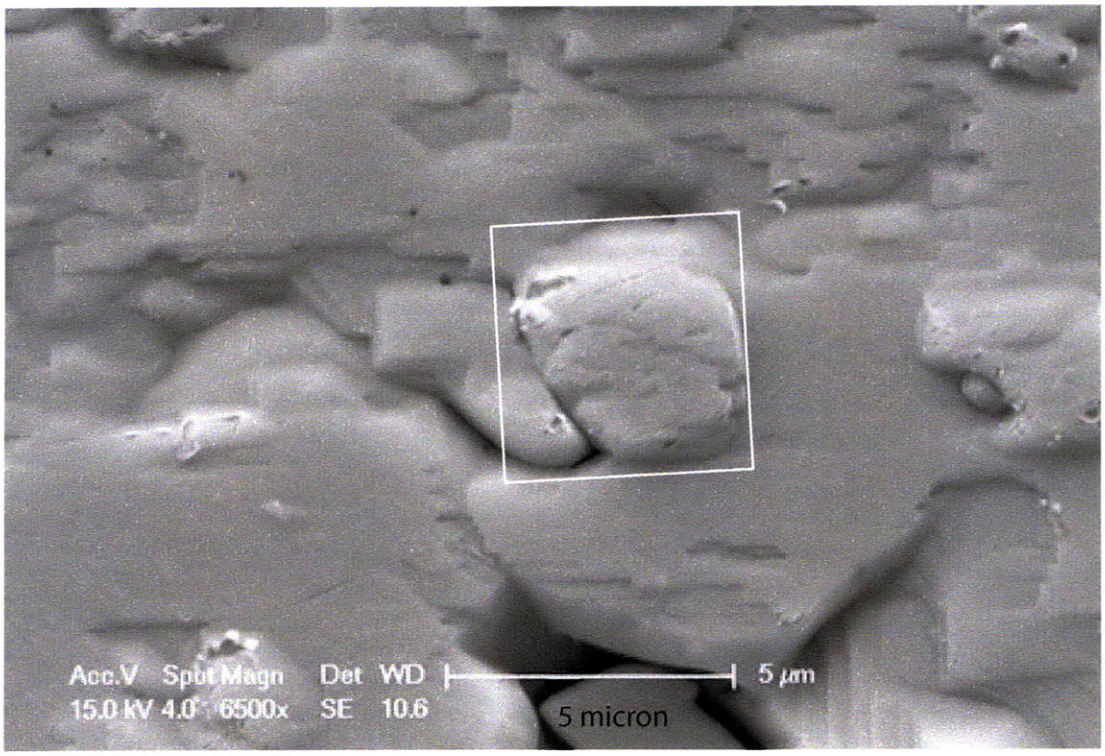

(b)

Figure 4-14:

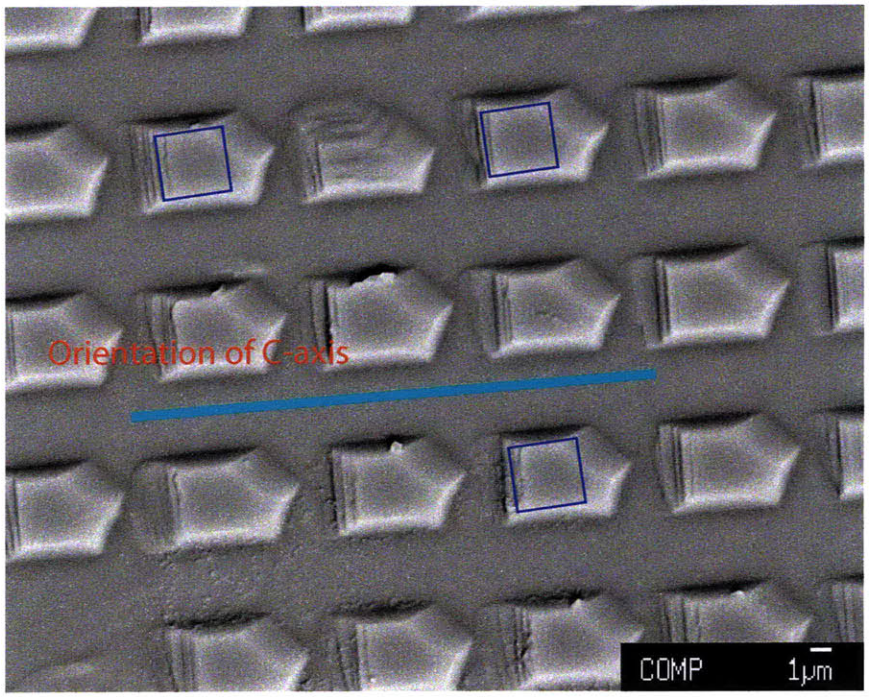

Figure 4-15:

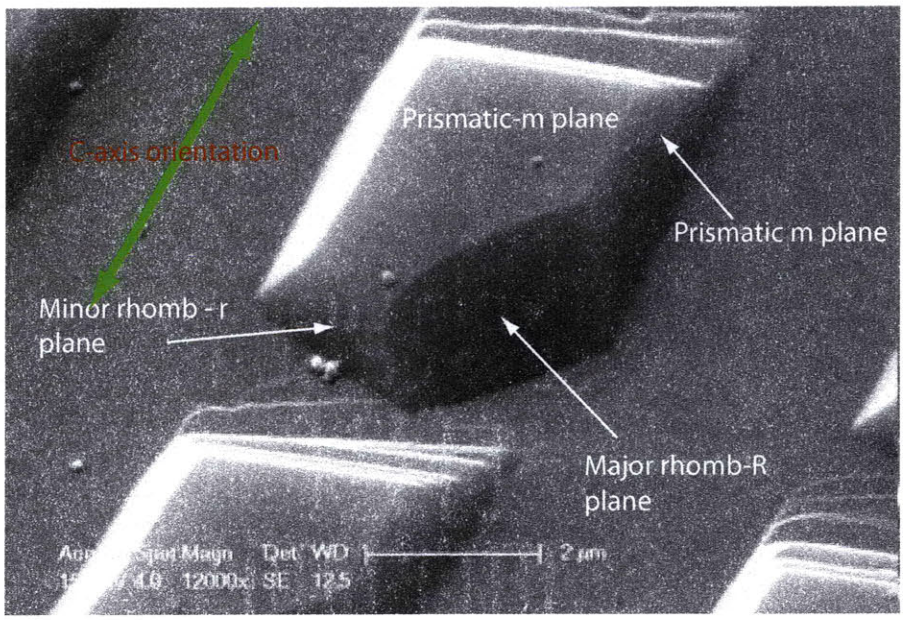

Figure 4-16:

Chapter 5

Discussion and Conclusions

5.1 Discussion

5.1.1 Grain Boundary Structure

Grain boundary structure has a significant role in the kinetics of pressure solution. As discussed in the first chapter, the grain boundary is envisaged to have either 1) a continuous thin fluid-film, allowing dissolved material to diffuse into the pore space, or 2) a dynamically stable island-channel structure. Models that support diffusion-limited pressure solution (Rutter & Elliott, 1976 ; Gratz, 1991 ; Gratier et al., 2009) propose that the grain boundary has a structured continuous fluid-film capable of transferring the normal stress. Arguing that the diffusivity of thin fluid-films is not high enough to explain geologically observed strain rates at temperatures below 200^0C, Gratz (1991) proposed that the grain boundaries might have interconnected cracks that would decrease the diffusion path lengths of fluid-film diffusion. On the other hand, the models suggesting that interfacial solution kinetics are rate limiting (Raj, 1982 ; Schutjens, 1991 ; Niemeijer et al., 2002 ; Noort, Spiers, & Pennock, 2008), assume that the underlying boundary structure is a dynamically stable island-channel structure and that structured thin fluid-films do not exist. In these island-channel models, material is dissolved due to free face dissolution on the lateral surfaces of the pillars and the base of the channels and is transported out

into pore space via bulk fluid diffusion through the channels. Since diffusivity of solute in the channels is often assumed to be equal to free-fluid diffusivity, diffusion is often assumed not be rate-limiting. However, the existence of dynamically stable island-channel structures has still not been conclusively demonstrated.

The wettability of grain boundaries depends on the relative energies of the grain boundaries and the solid/fluid interfaces. Fluid wets the grain boundary and forms a continuous fluid-film if twice the solid/liquid interface energy, γ_{SL}, is less than the grain boundary energy, γ_{GB}, i.e., $2 \times \gamma_{SL} \leq \gamma_{GB}$. The limiting condition, $2 \times \gamma_{SL} = \gamma_{GB}$, corresponds to a zero wetting angle, i.e., the angle formed between the two solid / liquid boundaries at the junction with the grain boundary). Thus, the fluid penetrates the grain boundary only if the wetting angle of the liquid and the solid is zero (Smith, 1948). When the wetting angle is greater than zero, the pore fluid will reside as discrete pockets in the grain boundary (fluid inclusions).

Farver (1992) demonstrated that the diffusivity of O_2 in novaculite (quartz) grain boundaries varied by 4 to 5 orders of magnitude, depending on whether the fluid was wetting (6M NaCl) or non-wetting (pure H_2O, pure CO_2). Although water against quartz has a wetting angle close to zero at room temperature, it increases with temperature (Stepanov et al., 1977). In another set of experiments, Watson & Brenan (1987) showed that, at elevated temperatures and pressures, pure H_2O does not wet quartz grain boundaries. In our experiments, we did not observe any evidence of thin fluid-films. Rather, in experiment PS052009, the tops of the pillars appeased to bond with the lens. The recovered micro-structure of the pillars showed pits resembling fluid inclusions (see Figure 4-11). Previously, Beeler & Hickman (1999) pressed quartz lens against a polished quartz flat at similar conditions and observed neck growth and formation of fluid inclusions under the contact, suggesting a non-zero wetting angle at the experimental conditions using pure water. However, fluid chemistry can play an important role in wetting the grain boundary, and a more fluid lain boundary might exist when electrolyte solutions are used. Previous studies reported that the addition of solutes like NaCl, KCl, CaF_2, Na_2CO_3 to water reduces the wetting angle drastically (Watson & Brenan, 1987 ; Farver & Yund, 1992). Future

experiments should be designed to explore this effect.

The fabricated structures on top of the quartz flats corresponded to the three types of boundary morphologies discussed above. In experiment PS031209, there was a fine crack running through the center of the contact (Figure 4-3). Similarly, there was a larger channel (Figure 4-4) running through the center of the contact (Figure 4-4) in experiment PS041309. Here, the channel was large enough (about 1μ m deep) to have free-fluid diffusivity. Both these surface structures represent variations on Gratz's grain-boundary model. Further, the island-channel structures are also an end member of Gratz's grain-boundary model. In the case of the regular island-channel structure, the diffusion length from grain boundary to channels was reduced to half the pillar width. However, convergence was observed only in experiment PS062309. And in this case, the convergence rate in experiment PS062309 was less than the convergence rate predicted by diffusion limited pressure solution (see section 5.1.3) and appears mainly due to crushing of the pillars, perhaps rate-limited by sub-critical crack growth (as discussed below). As we discussed earlier, the grain boundary appears not be wetted and fluid-film diffusion or Gratz type pressure solution did not occur.

The island-channel model does not require a fluid film on top of the islands. The dissolution occurs at the pillar sides and channel surfaces and maintains the island-channel structure dynamically (Noort, Visser, & Spiers, 2008). On the other hand, surface tension tries to heal the island-channel structure. Balancing both the driving forces, Noort (2008) suggested that island-channel structures might be dynamically stable if the normal stress is above a critical normal stress, σ_{cr} given by:

$$\sigma_{cr} = 2\alpha\sqrt{E\frac{\gamma_{sl}}{\delta}(\cos\frac{\theta}{2} - \cos\frac{\theta_{eq}}{2})} \tag{5.1}$$

where α is the ratio of the contact area occupied by islands to the total contact area, θ is the dihedral angle, θ_{eq} is the equilibrium dihedral angle and δ is the grain boundary thickness (in an island-channel model, it is the height of the islands). We took $\gamma_{sl} = 0.145$ J/m^2 (at 300^0C, from Noort (2008)), ($\cos\frac{\theta}{2} - \cos\frac{\theta_{eq}}{2}$)=0.17 (from Noort (2008)),

E = 95600 MPa and $\alpha = 0.25$. The value of γ_{sl} taken here gives a conservative estimate of the critical stress because γ_{sl} likely decreases with temperature. Using the above values, we calculated the critical normal stress, σ_{cr}, for island-channel structures in experiments PS052009 ($\delta = 1.05\mu$m) and PS062309 ($\delta = 0.55\mu$m) to be 24 MPa and 33 MPa, respectively. The mean normal stress at the start of our experiments, accounting for the area occupied by the channels, was approximately 80 MPa, which is greater than σ_{cr} for both the experiments. Moreover, the parameters of the island channel structures in the experiments were comparable to the island-channel structures envisaged (see Table 5.1).

Parameters	Values		
	Exp. PS052009	Exp. PS062309	Suggested by Noort,2008
Density of islands, M (m^{-2})	3.9×10^9	1.56×10^{10}	$10^{10} - 10^{13}$
α	0.25	0.25	0.2-0.5
δ (μ m)	1.05	0.55	$10^{-3} - 10^{-1}$

Table 5.1: Comparison of the island-channel structure parameters with values suggested by Van Noort

However, there was no convergence in experiment PS052009. Indeed, the pillars inside the contact showed signs of healing and tend to form fluid inclusion like structures (see Figure 4-11). The top of the pillars bonded with the lens indicating non-zero wetting angle. There was no significant free-face dissolution of the pillars or channels and in fact, the pillars grew even though there was no pressure solution.

In the only case where the lenses converged, the contact region showed significant crushing of pillars, micro-fracturing and micro-granulation. The pillar remnants appeared to be dissolved away with time. We did not see significant free-face dissolution on channel beds to suggest that an island-channel structure was being established. Also, the failure of the 4μm size pillars, while 8μm size pillars survived, indicates that smaller islands may not be able to sustain large normal stresses. Thus, it is possible that if sufficient time was allowed, the boundary might have healed. Finally, although Noort (2008) argued that the islands can take higher normal stresses (of the order of GPa) than observed in PS062309, this argument was based on indenter experiments and the two cases are not comparable. In indenter experiments, when an indenter

is pressed against a polished flat surface, the material surrounding the region under the indenter acts as a confining medium and enhances the strength. For the islands, there is effectively no confinement and pillars are loaded under uni-axial compression. Thus, they are prone to fail more easily.

5.1.2 Surface Damage

The geometries of the island-channel structures in experiments PS052009 and PS062309 were scaled to ensure equal mean normal stress in both experiments. Even, numerical simulations suggested a similar stress distribution in both the cases (section 3.4). The height was also scaled to ensure comparable bending stresses at the bottom of the pillars. However, during the experiments, the 4μm sized pillars failed while the 8 μm size pillars remained intact. The cause of the failure is not clear. Perhaps smaller pillars at the center of the contact failed in progression, owing to the tangential stresses imposed during sample assembly. The pillars might also have been damaged due to the rolling of the lens, as the temperature and pressure were raised to the design values. This rolling have sheared or damaged the smaller pillars more easily than the larger ones. Once, some pillars fail at the center of the contact, the surrounding pillars take more normal stresses and fail in turn.

During the experiments, the plano-convex lens rested with its convex side pressed against the quartz flat while the load was applied on the back through the tip of the gold wire (see Figure 2-4). This configuration is not stable and small disturbances might roll the lens back and forth. Transferring the load on to the lens through a larger contact might stabilize the system and in future experiments, the tip of the gold wire may be modified to be a disc with diameter close to the lens diameter.

As a secondary effect, the plasma etching on the quartz flats causes surface damage. Previous studies have shown that plasma etching can cause 40 nm diameter and 40 nm deep conical pits on the etched surface (Pantchev et al., 1983). The density of the defects (about 4×10^{14}) was reported to be independent of the etch rates and crystal orientation. Unfortunately, we did not characterize the quartz flats under SEM/TEM before the experiments. In any case, if there was a damage zone, the

4μm structure would see more damage since it had more exposed surface area. It is possible that the greater surface damage might lead to the preferential cataclastic failure of the 4μm pillars when compared to the 8μm. In the future, quartz flats might be treated with HF acid after the plasma etch to remove any damage zone on the surface.

5.1.3 Deformation Mechanism

Classical models of pressure solution suggest that at a grain-grain contact, the convergence rate, $\frac{ds}{dt}$, is given by, either :

$$\frac{ds}{dt} = \frac{8C_{eq}D_b\delta {V_s}^2 p_m}{RTd^2} \quad \text{when diffusion is rate-limiting (Rutter \& Elliott, 1976)}$$

$$or$$

$$\frac{ds}{dt} = \frac{K_{dis}V_s p_m}{RT} \quad \text{when dissolution is rate-limiting (Raj, 1982)} \tag{5.2}$$

where p_m is the effective mean normal stress and 'd' is the diffusional path length. More recently, Lehner & Leroy (2004) suggested a creep law, considering the coupling of dissolution and diffusion. But, when either of the mechanisms dominate, the law reduces to one of the above equations, accordingly. Using the values listed in the table for the parameters, we estimated the convergence rates expected in our experiments, for both rate-limiting steps. Of these parameters, D_b is the most poorly known and estimates vary by orders of magnitude.

For experiment PS052009, taking the diffusion path length to be half the pillar width (d = 4μm), p_m=443 MPa and the convergence rates were estimated as 0.29μ m/hr and 0.088μm/hr for diffusion or dissolution rate-limited pressure solution, respectively. However, despite a resolution of 0.02μ m to measure convergence, we did not observe any convergence over a period of 477 hours. Therefore, we interpret that none of the mechanisms were active or D_b was much lower than assumed in our calculations. Similarly, for experiment PS062309, taking d = 2μm, p_m=417 MPa and the convergences rates were estimated as 1.14μm/hr (diffusion rate limiting) and

Parameters	Values
Molar Volume of Quartz ,V_s (m^3/mol)	2.27×10^{-5} *
Free fluid Diffusivity, D, (m^2/s)	$9 \times 10^{-7} \times exp(-\frac{15000}{RT})$ *
Grain Boundary Diffusivity, D_b, (m^2/s)	$10^{-3} \times D$ ***
Dissolution Rate Constant,K_{dis}(m/s)	$2.27 \times 10^{-(3.826+0.002028T+\frac{4158}{T})}$ *
Equilibrium Concentration,$C_{eq}(mol/m^3)$	31.5 **
Grain Boundary Thickness,δ(nm)	2
Universal Gas Constant, R (J/K/mol)	8.314472
Temperature, T (K)	698.15

* from Lehner and Leroy (2004)
** calculated from solubility data by Kennedy at 425^0C and 150 MPa fluid pressure,
*** from Bernabé (2007)

Table 5.2: Numerical values of parameters for PS creep models

0.084μ m/hr (dissolution rate limiting). But, the observed convergence rate at the start of the experiment was approximately 0.002μ m/hr. Even in this case, diffusion or dissolution did not appear to govern the convergence rate.

On the other hand, the convergence rate (see section 4.3) when plotted against the mean normal stress (see section 4.2) at each observation time gave a stress exponent of 5.1 ± 0.5 (Figure 5-1). The stress exponent, which should be linear in stress (see equation 5.2), is much too high for dissolution/diffusion limited pressure solution, perhaps indicating sub-critical crack growth to be the underlying mechanism (Atkinson, 1984). Moreover, the recovered micro-structures show micro-cracking and micro-granulation. Plastic deformation under the pillar could have contributed to the high stress exponent, too, although we don't have any means to determine the role of plastic deformation in the present experiments. Although, determining stress exponent from a single experiment is not robust, these results agree with several previous studies of aggregate compaction that suggested that micro-cracking and sub-critical crack growth might be important mechanisms under hydrothermal conditions. Karner (2008) did isotropic and triaxial compression experiments on St. Peter quartz sand stone up to 225^0 C. They reported that triaxial yield points at higher temperatures decreased with increase in temperature in a way consistent with sub-critical crack growth. The data showed acoustic activity proportional to the de-

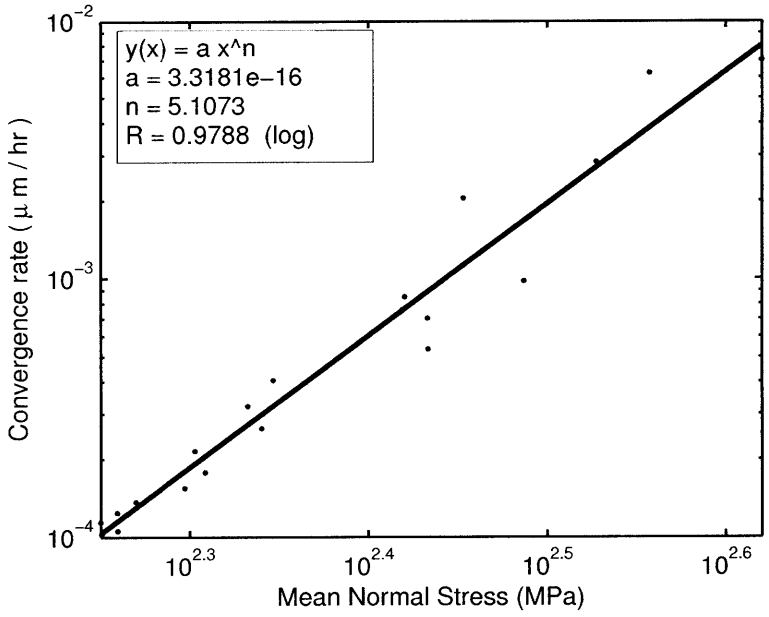

Figure 5-1: For experiment PS062309, convergence rate is plotted against mean normal stress on a log-log scale. As the lenses converge, the contact area increases and the mean normal stress decreases. Contact radius was estimated from the convergence at each observation point and the mean stress was calculated. The data fits to a power law with a stress exponent of 5.1 ± 0.5. We interpret this high stress exponent to be associated with sub-critical crack growth.

formation. Similar observations were made by Chester (2007) and Karner (2003) at lower temperatures. Noort (2008) performed iso-static compaction experiments on granular quartz at $300^0 - 600^0$C and 25-100 MPa of effect pressures. He reported extensive micro-cracking in the recovered micro-structures and grain size reduction from 129μm to 30μm due to micro-cracking and micro-granulation.

There is no robust model for aggregate compaction due to sub-critical crack growth. Thus, interpreting the aggregate experiments in terms of sub-critical crack growth is not straight forward. In general, various authors (Niemeijer et al., 2002 ; Noort, Spiers, & Pennock, 2008 ; Schutjens, 1991 ; Dewers & Hajash, 1995) attributed the observed compaction in aggregate experiments to pressure solution creep based on the activation energy (60-100 kJ/mol), grain size dependence (d^{-1}) and micro-structures, which are consistent with dissolution-limited pressure solution. An average stress exponent of 3 is usually reported in the aggregate compaction experiments.

However, the explanation for such high stress exponent is not satisfactory. On the other hand, sub-critical crack growth has similar activation energy and has higher stress exponent (Atkinson, 1984). Chester et. al (2007) reported a grain size dependence of d^{-1} for time-dependent compaction of quartz aggregates where sub-critical crack growth was dominant mechanism. Micro-structures resembling pressure solution can be produced even by micro-cracking, micro-granulation and subsequent dissolution. For example, Dickinson & Milliken (1995) examined the quartz rich, Etjo sand stone from nothern Namibia by cathodoluminescence imaging and showed that the concave-convex interpenetrating features associated with pressure solution may be due to micro-cracking. In their study, micro-cracks healed with authegenic cements at grain-grain contacts were visible under cathodoluminescence imaging.

However, we note that, Gratier's (2009) indenter experiments (at 350^0 C, 20 - 120 MPa of pore pressure and 25 -350 MPa of differential stress) on quartz crystal suggested diffusion controlled pressure solution and a stress exponent of 1.75. There are two significant differences between Gratier's experiments and this study. First, Gratier's indenter was steel (dissimilar solid phase boundary) and second, the fluid used was 1M NaOH (changes wettability and greatly enhances dissolution kinetics). The specific geometry of the indenter used by Gratier induces under-cutting at the edges and the observed convergence rates at least in part be due to this fact. In any case, the indenter experiments demonstrate that fluid chemistry and dissimilar solid boundaries are important aspects to be considered.

5.2 Conclusions

We did not observe evidence for classic pressure solution creep even though we tested several different possible boundary morphologies including: 1) a micro-crack through the contact, 2) a channel through the contact, and 3) island-channel structures fabricated at two different scales (4μm and 8μm). The quartz surfaces approach to bond with each other and form fluid inclusions similar to that observed by Hickman & Evans (1991) in halite-halite contacts. The island-channel structures in the experiments were

comparable in dimension to the island-channel structures suggested by previous workers in natural grain-grain boundaries. However, even though mean normal stresses on our island channel structures were well above the critical stresses suggested by Noort (2008) for dynamically stable island-channel structures, the island-channels did not appear to be dynamically stable, and in one case, the pillars (islands) in the contact grew, forming structures similar to fluid inclusions. We suggest that over-growth features and healing/precipitation features in micro-structures need not always indicate pressure solution. In the only case where convergence was observed, the recovered micro-structures indicated wide spread micro-cracking and crushing of pillars. The convergence rate followed a power law with a stress exponent of 5, perhaps suggesting that the dominant mechanism was sub-critical crack growth rather than pressure solution creep, although solid state-dislocation creep cannot be ruled out as factor.

Finally, we must observe that our conclusions are applicable to quartz-quartz boundaries at hydrothermal conditions in the presence of water that is saturated only with respect to silica. Presence of alkali ions or dissimilar solid grain boundaries might enhance wettability and may lead to true pressure solution. This would be good topic for future research.

Chapter 6

Future Work

Though we took measures to mis-orient the grain boundaries in the present experiments, we did not observe deformation by 'true' pressure solution. We suspect that the lack of fluid-film at the inter-granular boundary reduces the diffusion coefficient to very small values. We may be able to create favorable conditions for grain boundary wetting, either by decreasing the solid-liquid interfacial energy (γ_{sl}) or by increasing the solid-solid interfacial energy (γ_{gb}). γ_{sl} can be decreased by adding solutes like NaCl, KCl, CaF_2, Na_2CO_3 (Watson & Brenan, 1987 ; Farver & Yund, 1992). However, this may also change the dissolution kinetics. It is well known that Na enhances the dissolution rate multi-fold (Gratier et al., 2009). We can increase the solid-solid interfacial energy by increasing the grain boundary mis-orientation or by having dissimilar solid phase boundaries. So, the next step should be to try dissimilar materials. Sapphire is a good choice because it is harder than quartz and has relatively lower solubility and sluggish dissolution kinetics. The next experiment should be to press a sapphire lens against a quartz flat with a 8μ m island-chanel structure. Since, the channels are large enough, the pillar size determines the diffusion path length. If we observe convergence in this case, we should try increasing the pillar sizes and verify that the convergence rate varies proportional to the square of the pillar size. In these experiments, I expect the convergence rate to be constant until the pillars are dissolved and then to drop suddenly to a much lower value due to the sudden increase in the diffusion path length. It will be interesting to fabricate an island-channel struc-

ture on sapphire to see if the convergence rate is constant through out, since the roughness on sapphire is not eroded with time. On the other hand, different set of experiments at quartz-quartz contacts, varying the fluid chemistry (add electrolytes) would help us understand the pressure solution process in natural settings better. It would be interesting to see if addition of Na will lead to under-cutting or as well lead to true pressure solution at enhanced rates.

The other new experiment to try would be to repeat the experiment on 4μm pillar geometry with no pore fluid (dry). This checks indentation creep via dislocation creep and, if none were found, would strengthen the conclusion about cataclysis being rate limiting in 4μ case. Further into the future, the influence of presence of clays on PS rates can be tested by using a quartz flat coated with a thin clay layer.

It is worth mentioning here that the plano-convex sapphire lens to be used in the experiments proposed above, should have a larger radius of curvature than the quartz lens used in the present experiments. The benefits are two fold. Firstly, since sapphire has a young's modulus at least 3 times greater than quartz, using the same radius of curvature would cause larger stresses on the pillars and they may fail. Because it is possible to estimate the radius of curvature, from Hertzian contact theory, it should be possible to design the experiments, so that the quartz pillars would experience a stress state similar to that of the quartz-quartz experiments. Secondly, using a lens with larger radius of curvature would increase the resolution of our convergence measurements.

Appendix A

Fabrication Process

The recipe followed for fabricating the structure on the quartz flats is described below. All the steps were carried inside the clean room at Stanford Nano Fabrication facility (SNF). The process is pictorially depicted in the Figure A

- The quartz flats (Plano-Plano lens) were cleaned with Acetone and Isopropanol to remove any organic compounds present on the surface. Then, they were dried using a Nitrogen gun.

- A $840A^0$ thick Cr layer was vapour deposited on these clean samples at a rate of $6.7A^0$/sec.*Innotec ES26C E-Beam Evaporator* was used for the Cr deposition.

- The flats were then subjected to Vapor Prime in 'Yes oven' for 30 min. In the 'Yes oven', the flats were heated to 150^0C to evaporate any fluid on the surface of the flats and then HMDS (Hexamethyldisilazane) was deposited on the surface. This would make the surface hydrophobic and enhance the surface adhesion of the resist to the oxide/metal on the surface.

- *Shipley Photoresist 3612* was then coated over the vapor primed Cr layer at a spin rate of 3400 rpm for 1 minute to achieve a target thickness of 1.6μm. After spinning the photo-resist, the quartz flats were baked at 90^0C for 5 min on a pan. When an oven was used, the flats were allowed to bake for 30 min at 90^0C. This helped to harden the resist.

- The flats were aligned with the respective grid pattern on the Photo-Mask and exposed to UV light for 2 sec.*Karlsuss Contact Aligner* was used for aligning and exposure. A soft contact with 0.2 bar pressure was maintained between the mask and the quartz flats. The Cr side of the Photo-Mask touched the resist coated surface of the flats.

- Quartz flats were then prebaked (prior to development) in an oven for 20 minutes at 90^0C. And then, they were developed for 90 seconds in MF-26A (standard developer) and rinsed in water for 1 minute. After developing, the flats were post baked for 25 minutes in an oven.

- The flats with the developed photo-resist were dry etched with a plasma of Oxygen (25Watt, 150mT, O_2 20 sccm) for 30 seconds to remove any thin layer of resist that was masking the Cr layer along the pattern. Then, the flats were wet etched in standard Cr etchant (22% Ceric Ammonium Nitrate,9% Acetic Acid,69% water) for 50 seconds and rinsed in water for one minute. This process removed the Cr layer along the desired pattern.

- The flats were then cleaned for 5 minutes each in Acetone, Methanol and Isopropanol to strip off the residual resist. Cr thickness was measured on *Zygo White-Light 3D Surface Profiler* to ensure that the Cr layer was removed along the desired pattern.

- Now, the flats with the patterned Cr mask on the surface, were dry etched with a plasma of CHF_3 (100 standard cubic centimeters per minute , sccm) and O_2 (10 sccm) on *Drytek4*, an inductively coupled plasma etching machine.*Drytek4* was operated at 150 mT (milli Torr) pressure, 150W power and 310-330V voltage. This etched the quartz flats along the pattern, not protected by the Cr mask. The etch rate was observed to be 0.2μm/10 minutes. For 0.5μm target depth, flats were etched for 24 min and 48 min for 1μm target depth.

- This step was followed by dry etching again with a plasma of O_2 (150 watt, 150 mT, 20sccm) for 5 minutes to remove polymer (bi product of dry etching

of quartz) deposited on the surface. The thin layer of polymer could prevent Cr mask from being wet etched.

- The residual Cr mask on the surface was removed by wet etching in Cr etchant for 3-5 min.

- The flats were again cleaned with acetone, methanol and isopropanol, in the order.

- The fabricated structure was then characterised on *Zygo*. All the processes from vapor-prime to post-development bake were done in a litho room.

- The photo-mask (5x5x0.09 $inch^3$ soda lime plate) used for photolithography has 5 different patterns. Each pattern allows light to pass through a grid of lines. The lines in all the five patterns are spaced, center to center, twice their width apart. The region enclosed between lines is a square of side equal to the width of the lines. So, within a macroscopic square we have $\frac{3}{4}$ of the area was exposed in all the patterns. The patterns differ in the width of the lines (4μm,5μm,8μm,12μm,16μm) and thus the spacing. The photo-mask has two copies of each pattern except for the 16μm pattern. Thus, a total of nine patterns are present on the photo-mask.

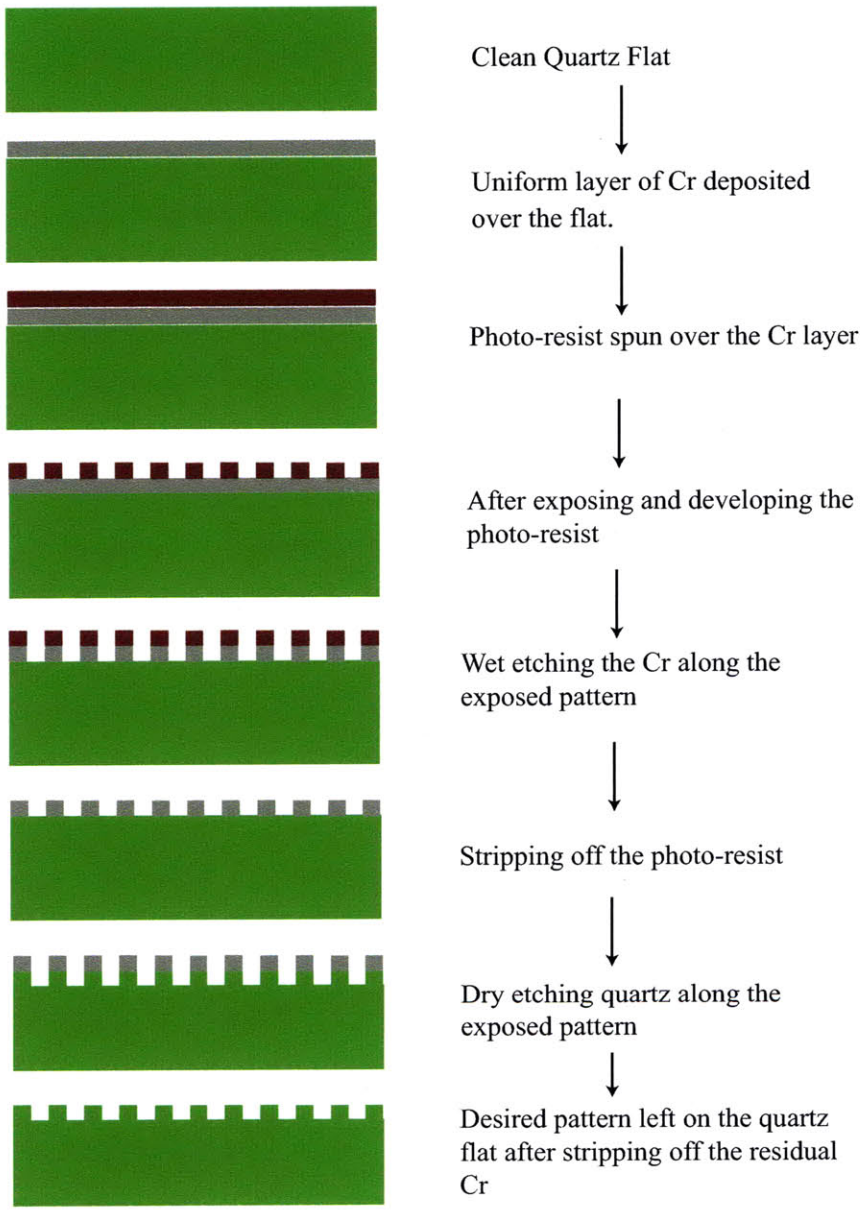

Figure A-1: Fabrication procedure

Appendix B

Sample Dimensions

(a) Surface structure on dry etched flats. Refer to Figure B-1 for reading the table

Quartz Flat	$h_0(\mu m)$	$p_t(\mu m)$	$p_b(\mu m)$	$c_t(\mu m)$	$c_b(\mu m)$
Sample 2	1.05±0.005	8.3±0.1	10.6±0.1	8.3±0.1	6.0±0.1
Sample b1	1.025±0.005	7.2±0.1	9.9±0.1	8.8±0.1	6.1±0.1
Sample c2	1.00±0.01	6.6±0.1	9.4±0.1	9.4±0.1	6.6±0.1
Sample a2	1.04±0.005	5.7±0.3	9.1±0.3	10.2±0.3	6.9±0.3
Sample c1	0.55±0.005	4.0±0.1	4.9±0.1	4.0±0.1	3.1±0.1
Sample b2	0.57±0.005	3.5±0.1	4.6±0.1	4.5±0.1	3.4±0.1
Sample a1	0.57±0.005	4.4±0.1	5.4±0.1	3.6±0.1	2.6±0.1
Sample d	0.45±0.005	3.5±0.1	4.4±0.1	4.5±0.1	3.6±0.1

(b) Dimensions of Triangular Etch Pits on wet etched flat

Quartz Flat	sides of triangular	etch pits (μm)	depth (μm)
Sample 5	35±10	60±10	60±10	1±0.2

Table B.1: Surface structure on fabricated samples.

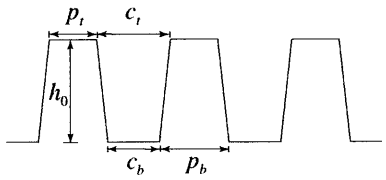

Figure B-1: Profile of fabricated island-channel structure

Références

Atkinson, B. (1984). Subcritical crack growth in geological materials. *Journal of Geophysical Research, 89-B6*, 4077-4114.

Bathurst, R. (1958). Diagenetic fabrics in some british dinantian limestones. *Liverpool Manchester Geological Journal, 2*, 11-36.

Beeler, N., & Hickman, S. (1999). The effect of grain boundary structure on the rate of quartz pressure solution. *Eos Trans. AGU, 80*.

Beeler, N., & Hickman, S. (2004). Stress-induced, time-dependent fracture closure at hydrothermal conditions. *Journal of Geophysical Research, 109*, B02211.

Bernabe, Y., & Evans, B. (2007). Numerical modelling of pressure solution deformation at axisymmetric asperities under normal load. *Geological Society, London, Special Publications, 284*, 185-205.

Bos, B., Peach, C., & Spier, C. (2000). Slip behavior of simulated gouge-bearing faults under conditions favoring pressure solution. *Journal of Geophysical Research, 105, no. B7*, 16699-16717.

Chester, F., Chester, J., Kronenberg, A., & Hajash, A. (2007). Subcritical creep compaction of quartz sand at diagenetic conditions: Effects of water and grain size. *Journal of Geophysical Research, 112*, B06203.

Chester, J., Lenz, S., Chester, F., & Lang, R. (2004). Mechanisms of compaction of quartz sand at diagenetic conditions. *Earth and Planetary Science Letters, 220*, 435-451.

Cox, S., & Paterson, M. (1991). Experimental dissolution-precipitation creep in quartz aggregates at high temperatures. *Geophysical Research Letters, 18, no. 8*, 1401-1404.

De Boer, R. (1977). On the thermodynamics of pressure solution interaction between chemical and mechanical forces. *Geochimica et Cosmochimica Acta, 41*, 249-256.

Dewers, T., & Hajash, A. (1995). Rate laws for water-assisted compaction and stress-induced water-rock interaction in sandstones. *Journal of Geophysical Research, 100, no. B7*, 13093-13112.

Dickinson, W., & Milliken, K. (1995). The diagenetic role of brittle deformation in compaction and pressure solution , etjo sandstone, namibia. *The Journal of Geology, 103*, 339-347.

Durney, D., & Ramsay, J. (1973). Incremental strains measured by syntectonic crystal growths, in gravity and tectonics. In (p. 67-96). Wiley, New York.

Farver, J., & Yund, R. (1992). Oxygen diffusion in a fine-grained quartz aggregate

with wetted and nonwetted microstructures. *Journal of Geophysical Research, 97, no. B10*, 14,017-14,029.

Gratier, J., & Guiguet, R. (1986). Experimental pressure solution-deposition on quartz grains:the crucial effect of the nature of the fluid. *Journal of Structural Geology, 8, no. 8*, 845-856.

Gratier, J., Guiguet, R., Renard, F., Jenatton, L., & Bernard, D. (2009). A pressure solution creep law for quartz from indentation experiments. *Journal of Geophysical Research, 114*, B03403.

Gratier, J., Muquet, L., Hassani, R., & Renard, F. (2005). Experimental microstylolites in quartz and modeled application to natural stylolitic structures. *Journal of Structural Geology, 27*, 89-100.

Gratz, A. (1991). Solution-transfer compaction of quartzites: Progress toward a rate law. *Geology, 19*, 901-904.

Groshong, R. (1988). Low-temperature deformation mechanisms and their interpretation. *Geol. Soc. Am. Bull., 100*, 1329-1360.

He, W., Hajash, A., & Sparks, D. (2007). Evolution of fluid chemistry in quartz compaction systems: Experimental investigations and numerical modeling. *Geochimica et Cosmochimica Acta, 71*, 4846-4855.

Hickman, S., & Evans, B. (1991). Experimental pressure solution in halite: the effect of grain/interphase boundary structure. *Journal of the Geological Society, 148*, 549-560.

Hickman, S., & Evans, B. (1992). Growth of grain contacts in halite by solution-transfer: Implications for diagenisis, lithification, and strength recovery [In]. In (p. 253-280). Academic Press.

Hickman, S., & Evans, B. (1995). Kinetics of pressure solution at halite-silica interfaces and intergranular clay films. *Journal of Geophysical Research, 100, no. B7*, 13113-13132.

Hickman, S., Sibson, R., & Bruhn, R. (1995). Introduction to special section: mechanical involvement of fluids in faulting. *Journal of Geophysical Research, 100, no. B7*, 12831-12840.

Houseknecht, D., & Hathon, L. (1987). Petrographic constraints on models of intergranular pressure solution in quartzose sandstones. *Appl. Geochem., 2*, 507-521.

Israelachvili, J. (1986). Measurement of the viscosity of fluids in very thin films. *Journal of Colloid and Interface Science, 110*, 263-271.

Iwasaki, F., iwasaki, H., & Okabe, Y. (1997). Growth rate anisotropy of synthetic quartz grown in na_2co_3 solution. *Journal of Crystal Growth, 178*, 648-652.

Johnson, K. (1985). Contact mechanics. In (pp. 60,93). Cambridge University Press.

Karner, S., Chester, F., Chester, J., & Hajash, A. (2008). Hydrothermal deformation of granular quartz sand. *Journal of Geophysical Research, 113,B05404*.

Karner, S., Chester, F., Kronenberg, A., & Chester, J. (2003). Subcritical compaction and yielding of granular quartz sand. *Tectonophysics, 377*, 357-381.

Kennedy, C. (1950). A portion of the system silica-water. *Economic Geology, 45*, 629-653.

Lehner, F. (1985). A model for intergranular pressure solution in open systems. *Pure Applied Geophysics, 122*, 53-85.

Lehner, F., & Bataille, J. (1995). Nonequilibrium thermodynamics of pressure solution. *Tectonophysics*, *245*, 153-170.

Lehner, F., & Leroy, Y. (2004). Sandstone compaction by intergranular pressure solution. gué guen, y. and bouté ca, m. (eds) mechanics of fluid-saturated rocks. *International Geophysics Series*, *89*, 115-168.

Luan, F., & Paterson, M. (1992). Preparation and deformation of synthetic aggregates of quartz. *Journal of Geophysical Research*, *97, no. B1*, 301-320.

McClay, K. (1977). Pressure solution and coble creep in rocks and minerals: a review. *Journal of the Geological Society*, *134*, 57-70.

Nakashima, S. (1995). Diffusivity of ions in pore water as a quantitative basis for rock deformation rate estimates. in: C.j. spiers and t. takeshita (editors), influence of fluids on deformation processes in rocks. *Tectonophysics*, *245*, 185-203.

Niemeijer, A., & Spiers, C. J. (2002). Compaction creep of quartz-muscovite mixtures at 500^0 c: Preliminary results on the influence of muscovite on pressure solution. *Geological Society,London, Special Publications*, *200*, 61-71.

Niemeijer, A., Spiers, C. J., & Bos, B. (2002). Compaction creep of quartz sand at $400 - 600^0$c: experimental evidence for dissolution-controlled pressure solution. *Earth and Planetary Science Letters*, *195*, 261-275.

Noort, R., Spiers, C., & Pennock, G. (2008). Compaction of granular quartz under hydrothermal conditions: Controlling mechanisms and grain boundary processes. *Journal of Geophysical Research*, *113*, B12206.

Noort, R., Visser, H., & Spiers, C. (2008). Influence of grain boundary structure on dissolution controlled pressure solution and retarding effects of grain boundary healing. *Journal of Geophysical Research*, *113*, B03201.

Pantchev, B. G., MIkhailov, M. G., & Danesh, P. (1983). Surface relief of crystalline quartz etched in a planar plasma reactor. *Thin Solid Films*, *106*, 136-144.

Pashley, R. (1981). Hydration forces between mica surfaces in aqueous electrolyte solution. *The Journal of Colloid and Interface Science*, *80*, 153-162.

Pashley, R., & Israelachvili, J. (1984). Molecular layering of water in thin films between mica surfaces and its relation to hydration forces. *The Journal of Colloid and Interface Science*, *101*, 511-523.

Paterson, M. (1973). Non hydrostatic thermodynamics and its geological applications. *Rev. Geophys. Space Phys.*, *11*, 355-390.

Pharr, G., & Ashby, M. (1981). On creep enhanced by a liquid phase. *Cambridge Univ. Eng. Dept. Research Report.*

Raj, R. (1982). Creep in polycrystalline aggregates by matter transport through a liquid phase. *Journal of Geophysical Research*, *87, no. B6*, 4731-4739.

Renard, F., Ortoleva, P., & Gratier, J. (1997). Pressure solution in sandstones: influence of clays and dependence on temperature and stress. *Tectonophysics*, *280*, 257-266.

Rimstidt, J., & Barnes, H. (1980). Kinetics of silica-water reactions. *Geochimica et Cosmochimica Acta*, *44*, 1683-1699.

Rutter, E. (1983). Pressure solution in nature, theory and experiment. *Journal of the Geological Society, London*, *140*, 725-740.

Rutter, E., & Elliott, D. (1976). The kinetics of rock deformation by pressure solution. *Philisophical Transactions of the Royal Society*, *283*, 203-219.

Rutter, E., & Mainprice, D. (1979). On the possibility of slow fault slip controlled by diffusive mass transfer process. *Gerlands Beitr. Geophysik, Leipzig*, *88*, 154-162.

Rutter, E., & Wanten, P. (2000). Experimental study of the compaction of phyllosilicate-bearing sand at elevated temperature and with controlled pore water pressure. *Journal of Sedimentary Research*, *70, no. 1*, 107-116.

Schutjens, M. (1991). Experimental compaction of quartz sand at low effective stress and temperature conditions. *Journal of the Geological Society , London*, *148*, 527-539.

Shimizu, I. (1995). Kinetics of pressure solution creep in quartz: theoretical considerations. *Tectonophysics*, *245*, 121-134.

Smith, S. (1948). Graina, phases and interfaces: an interpretation of microstructure. *Transaction of AIME*, *175*, 15-51.

Sorby, H. (1863). On the direct correlation of mechanical and chemical forces. *Proc. R. Soc., London*, *12*, 12,538-50.

Spiers, C., Schutjens, P. M. T. M., Brzesowsky, R. H., Peach, C. J., Liezenberg, J. L., & Zwart, H. J. (1990). Experimental determination of constitutive parameters governing creep of rocksalt by pressure solution, in deformation mechanisms, rheology and tectonics, edited by r. j. knipe and e. h. rutter. *Geological Society Special Publications , London*, *54*, 215-227.

Sprunt, E., & Nur, A. (1977). Experimental study of the effects of stress on solution rate. *Journal of Geophysical Research*, *82*, 3013-3022.

Stepanov, V. G., Volyak, L. D., & Tarlakov, Y. (1977). Wetting angles close to critical temperature. *Journal of Engineering Physics and Thermophysics*, *32-3*, 283-286.

Stockdale, P. (1926). The stratigraphic significance of solution in rocks. *Journal of Geology*, *34*, 399-414.

Stockdale, P. (1936). Rare stylolites. *American Journal of Science*, *32*, 129-133.

Tada, R., Maliva, R., & Siever, R. (1987). A new mechanism for pressure solution in porous quartzose sandstone. *Geochimica et Cosmochimica Acta*, *51,no 9*, 2295 - 2301.

Tada, R., & Siever, R. (1986). Experimental knife-edge pressure solution of halite. *Geochimica et Cosmochimica Acta*, *50,no 1*, 29-36.

Tada, R., & Siever, R. (1989). Pressure solution during diagenesis. *Annual Review of Earth and Planetary Sciences*, *17, no. 89*, 119.

Trurnit, P. (1968). Pressure solution phenomenon in detrital rocks. *Sediment. Geol*, *s 2*, 89-114.

Verma, M. (2003). Steam tables for pure water as an activex component in visual basic 6.0. *Computers and Geosciences*, *29*, 1155-1163.

Wagner, W., & Pruß, A. (2002). The IAPWS formulation 1995 for the thermodynamic properties of ordinary water substance for general and scientific use. *J. Phys. Chem. Ref. Data*, *31*, 387.

Watson, E., & Brenan, J. (1987). Fluids in the lithosphere, 1. experimentally-

determined wetting characteristics of co2-h20 fluids and their implications for fluid transport, host-rock physical properties, and fluid inclusion formation. *Earth and Planetary Science Letters*, *85*, 497-515.

Weyl, K. (1959). Pressure solution and the force of crystallization: A phenomenological theory. *Journal of Geophysical Research*, *64, no. 11*.

Zubutsov, S., Renard, F., & Gratier, J. (2005). Single-contact pressure solution creep on calcite monocrystals. *Geological Society, London, Special Publications*, *243*, 81-95.